JACS
JOURNAL OF THE AMERICAN CHEMICAL SOCIETY
Article
Cite This: J. Am. Chem. Soc. 2019, 141, 17703−17712
pubs.acs.org/JACS

Enhanced Gas Uptake in a Microporous Metal−Organic Framework *via* a Sorbate Induced-Fit Mechanism

Mei-Hui Yu,[†] Brian Space,[§] Douglas Franz,[§] Wei Zhou,[∥] Chaohui He,[⊥] Libo Li,[⊥] Rajamani Krishna,[#] Ze Chang,[†] Wei Li,[†] Tong-Liang Hu,*[,†] and Xian-He Bu*[,†,‡]

[†]School of Materials Science and Engineering, National Institute for Advanced Materials, Nankai University, Tianjin 300350, China
[‡]State Key Laboratory of Elemento-Organic Chemistry, and Collaborative Innovation Center of Chemical Science and Engineering, Nankai University, Tianjin 300071, China
[§]Department of Chemistry, University of South Florida, 4202 East Fowler Avenue, Tampa, Florida 33620, United States
[∥]NIST Center for Neutron Research, National Institute of Standards and Technology, Gaithersburg, Maryland 20899-6102, United States
[⊥]Shanxi Key Laboratory of Gas Energy Efficient and Clean Utilization, College of Chemistry and Chemical Engineering, Taiyuan University of Technology, Taiyuan, 030024 Shanxi, China
[#]Van 't Hoff Institute for Molecular Sciences, University of Amsterdam, Science Park 904, Amsterdam 1098, XH, The Netherlands

Supporting Information

ABSTRACT: Physical adsorption of gas molecules in microporous materials is an exothermic process, with desorption entropy driving a decrease in uptake with temperature. Enhanced gas sorption with increasing temperature is rare in porous materials and is indicative of sorbate initiated structural change. Here, sorption of C_2H_6, C_3H_6, and C_3H_8 in a flexible microporous metal−organic framework (MOF) $\{Cu(FPBDC)]\cdot DMF\}_n$ (**NKU-FlexMOF-1**) (H_2FPBDC = 5-(5-fluoropyridin-3-yl)-1,3-benzenedicarboxylic acid) that increases with rising temperature over a practically useful temperature and pressure range is reported along with other small molecule and hydrocarbon sorption isotherms. Single X-ray diffraction studies, temperature-dependent gas sorption isotherms, *in situ* and variable temperature powder X-ray diffraction experiments, and electronic structure calculations were performed to characterize the conformation-dependent sorption behavior in **NKU-FlexMOF-1**. In total, the data supports that the atypical sorption behavior is a result of loading-dependent structural changes in the flexible framework of **NKU-FlexMOF-1** induced by sorbate-specific guest−framework interactions. The sorbates cause subtle adaptations of the framework distinct to each sorbate providing an induced-fit separation mechanism to resolve chemically similar hydrocarbons through highly specific sorbate−sorbent interactions. The relevant intermolecular contacts are shown to be predominantly repulsion and dispersion interactions. **NKU-FlexMOF-1** is also found to be stable in aqueous solutions including toleration of pH changes. These experiments demonstrate the potential of this flexible microporous MOF for cost and energy efficient industrial hydrocarbon separation and purification processes. The efficacy for the separation of C_3H_6/C_3H_8 mixtures is explicitly demonstrated using **NKU-FlexMOF-1a** (i.e., activated **NKU-FlexMOF-1**) for a particular useful temperature range.

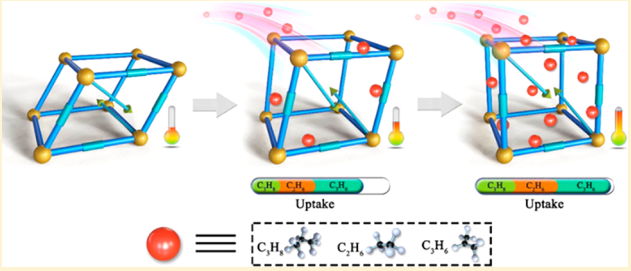

INTRODUCTION

Among various porous materials, metal−organic frameworks (MOFs), also known as porous coordination polymers, are a promising class of crystalline materials with voids or internal surface areas that have become a focus in both chemistry and materials science.[1−9] MOFs are inherently inorganic−organic hybrids with structural bond strengths that permit sorbate induced flexibility, distinguishing them from other porous solids.[10−12] Considering extant MOFs, about 100 of some 20 000 reported MOFs exhibit breathing or flexibility, making them exciting candidates for storage, selectivity, separations, and sensing.[13−22] The flexibility of MOFs can be attributed to many mechanisms, such as the rotation of the organic ligands, multiple accessible configurations of metal nodes and clusters, the sliding of interpenetrated subnetworks, and the inherent collective vibrational relaxation of a particular topology.[13,23] Reversible motions result from external stimuli including changes in temperature or pressure, the presence or removal of guest molecules, photoactive moieties, or electrical and magnetic interactions that trigger structural flexibility.[24,25] Understanding tailoring and exploitation of the dynamic phenomena occurring in flexible frameworks and their pores suggests tunable or desired properties that help realize the

Received: July 22, 2019
Published: October 11, 2019

DOI: 10.1021/jacs.9b07807
J. Am. Chem. Soc. 2019, 141, 17703−17712

promise of smart materials.[25] Therefore, focused efforts are underway to construct flexible MOFs and understand their structure−property relationships while tailoring them to specific aims.[10,11,25,26] For example, NH_2-MIL-53(Al) is a flexible MOF that when mixed with PSF Udel P-3500 forms a nanocomposite membrane that produces increased CO_2/CH_4 selectivity up to 77 with increased pressure. The mixed matrix membrane's (MMM) ability to achieve high selectivity was attributed to the dynamic behavior of NH_2-MIL-53(Al) particles.[27,28] In addition, the MOF $[Cu(aip)(H_2O)](solvent)_n$ (aip = 5-azidoisophthalate) selectively sorbs CO with adaptable pores; unprecedented high selectivity was achieved by CO molecules coordinating with copper(II) ions, resulting in a global transformation of the framework.[29] Flexible MOFs for light hydrocarbons applications, exhibiting selective sorption behavior, are desirable due to the importance of hydrocarbons as energy resources and commodity chemicals in the petrochemical industry.[4,30−36]

Here, a flexible microporous MOF $\{Cu(FPBDC)]\cdot DMF\}_n$ (**NKU-FlexMOF-1**) (H_2FPBDC = 5-(5-fluoropyridin-3-yl)-1,3-benzenedicarboxylic acid) was synthesized using $[Cu_2(COO)_4N_2]$ paddle-wheel SBUs and $FPBDC^{2-}$ ligands. The MOF, $[Cu(FPBDC)]$ (**NKU-FlexMOF-1a**), exhibits a guest-specific structural deformation of the flexible framework when activated. The material subtly adapts to each sorbent *via* an induced-fit mechanism where electronic repulsion and intermediate range dispersion interactions balance in a manner sufficiently distinct for each sorbate that the energetics allows for chemical resolution of similar species. To this point, as a result of the MOF's framework responding to the presence of sorbates, **NKU-FlexMOF-1a** exhibits inversely temperature enhanced sorption behavior for C_2H_6, C_3H_6, and C_3H_8 over a measured temperature range. Distinct from conventional gas adsorption behaviors inherent in rigid porous materials, the maximum saturated uptake amounts gradually increase with temperature in a practically useful temperature and pressure range, as suggested in Scheme 1 and demonstrated in Figure 2.

Scheme 1. On the Basis of the Strongly Guest-Triggered Structure Deformation of the Flexible Framework, the Framework Exhibits Inversely Enhanced Adsorption Behaviors for C_2H_6, C_3H_6, and C_3H_8

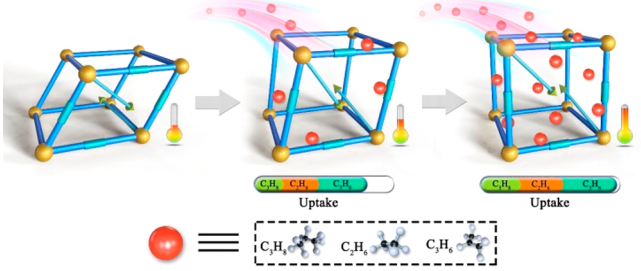

The unusual sorption behavior associated with the flexibility results from the framework adapting aptly with increased temperature to produce species-specific induced fits; **NKU-FlexMOF-1a** captures relatively larger amounts of C_3H_8 at a higher temperature and can efficiently separate C_3H_6/C_3H_8 at the lower temperatures studied while maintaining a recognizably similar sorbate−sorbent structure and associated physical interactions. It was found that the repulsion and dispersion interactions are determined by small structural changes and the electrostatic environment remains very similar for the related chemical sorbates (e.g., $C_2H_6/C_3H_6/C_3H_8$).

RESULTS AND DISCUSSION

Synthesis, Crystal Structure, and Stability of NKU-FlexMOF-1. The reaction of H_2FPBDC and $CuCl_2\cdot 2H_2O$ under solvothermal conditions produced a porous framework **NKU-FlexMOF-1**. Single-crystal X-ray diffraction analysis of **NKU-FlexMOF-1** (Table S1) showed that each Cu(II) ion is coordinated by four carboxylic oxygen atoms and one pyridine nitrogen atom from five $FPBDC^{2-}$ ligands and that the two adjacent Cu(II) ions constitute a $[Cu_2(COO)_4N_2]$ paddle-wheel SBU (Figure 1a). Each $FPBDC^{2-}$ ligand coordinates to

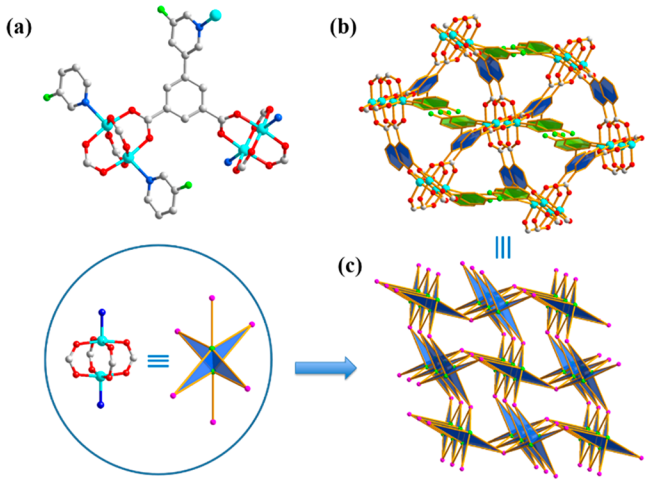

Figure 1. (a) Coordination environment of ligand $FBDC^{2-}$ and Cu(II). Key: Cu in turquoise, C in light gray, N in blue, O in red, and F in green. All H atoms were omitted for clarity. (b) 3D structure showing the narrow open triangular 1D channels. (c) Simplified 3D structure that suggests its continuous deformability *via* the "hinges".

three paddle-wheel SBUs, giving a three-dimensional (3D) coordination framework with narrow open triangular 1D channels along the *a*-axis (Figure 1b), similar to a previously reported MOF compound NJU-Bai7.[37] As shown in Figure 1b, two open triangular channels sharing the same open angle constitute a homologous rhombic channel along the *a*-axis (Figure 1c). The known flexibility of frameworks with rhombic channels led to investigating potential framework distortions in response to sorption.[38,39] Because there is a DMF molecule in its asymmetric unit, the occupied channels are sterically expanded. When the DMF molecules are removed, there is structural relaxation, consistent with the induced-fit properties of the material.

The solvent and thermal stabilities of **NKU-FlexMOF-1** were first demonstrated by PXRD and thermogravimetric (TG) analyses (Figures S1−S3). The TG curve and VT-PXRD patterns show that the thermal stability of **NKU-FlexMOF-1** extends to about 340 °C. As shown in the PXRD pattern (Figure S3), **NKU-FlexMOF-1** exhibits good stability to a wide pH range (3−11). After immersing in aqueous solutions with different pH values, the samples were analyzed by optical microscopy and scanning electron microscopy (SEM), demonstrating their crystalline state and stable morphology (Figures S4 and S5). The aqueous solutions were measured to assess the content of Cu^{2+} by ICP, which results in Table S4 show that there are only small pH-independent concentrations

DOI: 10.1021/jacs.9b07807
J. Am. Chem. Soc. 2019, 141, 17703−17712

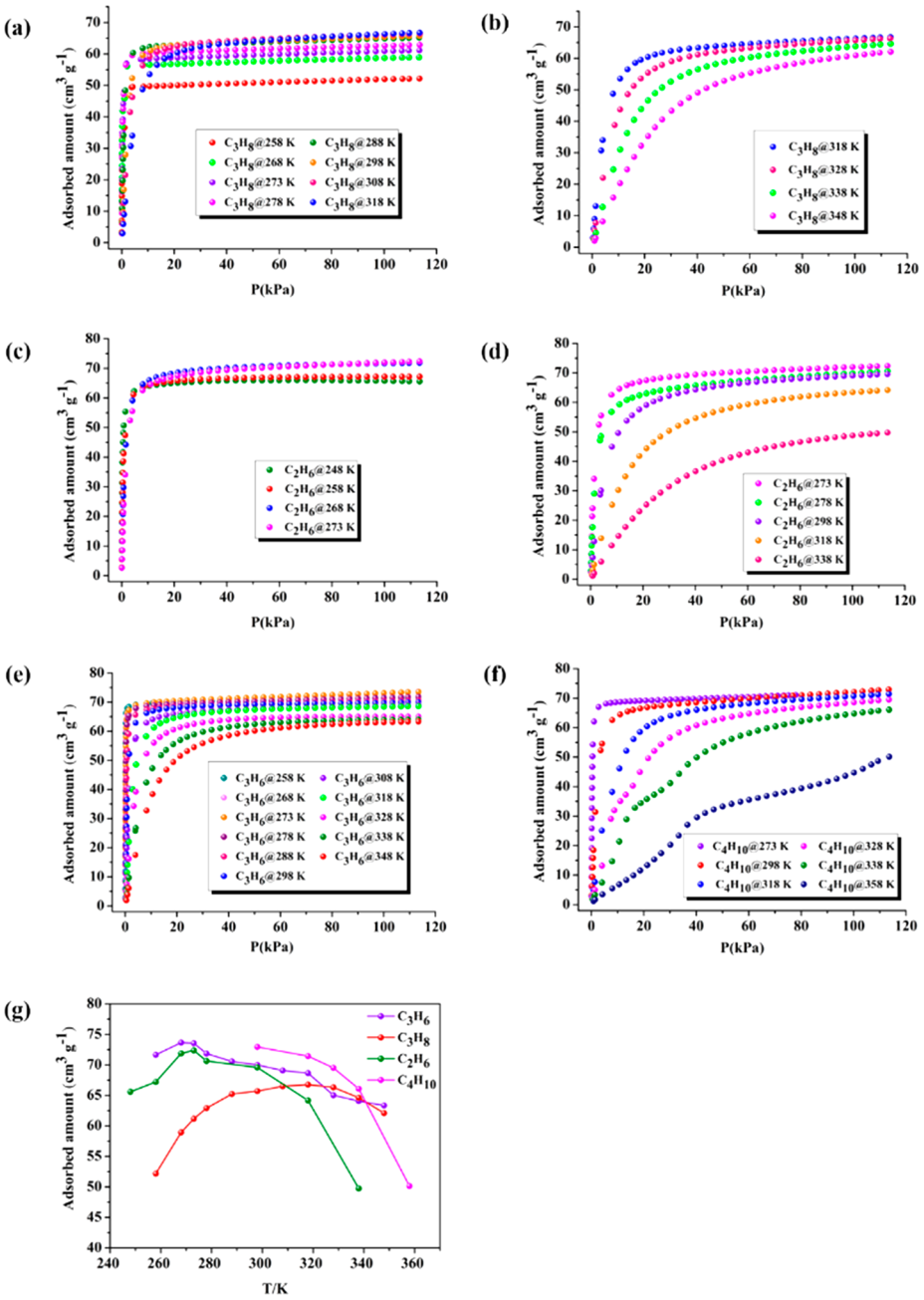

Figure 2. (a) C_3H_8 adsorption isotherms from 258 to 318 K. (b) C_3H_8 adsorption isotherms from 318 to 348 K. (c) C_2H_6 adsorption isotherms from 248 to 273 K. (d) C_2H_6 adsorption isotherms from 273 to 338 K. (e) C_3H_6 adsorption isotherms from 258 to 348 K. (f) C_4H_{10} adsorption isotherms from 273 to 358 K. (g) Temperature-dependent uptake amounts for C_2H_6, C_3H_6, C_3H_8, and C_4H_{10} demonstrating the enhanced uptake phenomenology.

of Cu^{2+}, confirming that **NKU-FlexMOF-1** has good stability in pH range 3−11. These robust properties, especially water stability, which is uncommon and highly desired for MOFs, make **NKU-FlexMOF-1** practically useful.

Gas Adsorption Properties of NKU-FlexMOF-1a. Prior to gas adsorption measurements, **NKU-FlexMOF-1** was activated by heating the material to 140 °C under a dynamic vacuum to obtain the desolvated **NKU-FlexMOF-1a**. At 77 K, N_2 adsorption measurements were then used to assess the porosity and structural flexibility. The evacuated Brunauer−Emmett−Teller and Langmuir surface areas of **NKU-FlexMOF-1a** were calculated to be 952 and 993 $m^2\ g^{-1}$, respectively (Figure S7). The N_2 adsorption isotherm exhibits a series of discrete steps apparent on a log plot at low pressure (Figure S6), indicating that **NKU-FlexMOF-1a** shrinks when solvent molecules are fully evacuated and responsively transforms to a series of expanded structures under increasing guest gas pressure, assuming a new conformation for each sorbed molecule. Thus, the transitions are gradual rather than an abrupt gated phenomena. At 1.0 bar, **NKU-FlexMOF-1a** reaches an expanded phase with a captured N_2 density of 270.9 $cm^3\ g^{-1}$ (3.9 mol mol^{-1}).

Next, single-component adsorption isotherms of guest-free **NKU-FlexMOF-1a** for N_2, CO_2, CH_4, C_2H_4, C_2H_6, C_3H_6, C_3H_8, and C_4H_{10} were measured at 273 and 298 K and other temperatures for selected species. As shown in Figures S8−

DOI: 10.1021/jacs.9b07807
J. Am. Chem. Soc. 2019, 141, 17703−17712

S14, with the increase of sorbate size, correlating with stronger dispersion interactions, the adsorption isotherms become steeper for very low pressures. Consider the empirical kinetic diameters are 3.3 Å (CO_2), 3.758 Å (CH_4), 4.163 Å (C_2H_4), 4.443 Å (C_2H_6), 4.678 Å (C_3H_6), 4.3−5.118 Å (C_3H_8), and 4.687 Å (*n*-butane).[40] Note that the larger gas sorbates with electron rich double bonds have stronger host−guest interactions between these molecules and the **NKU-Flex-MOF-1a** framework relative to those with single bonds; compared to molecules of similar size, the molecule with a double bond typically has a stronger binding with the framework *via* electrostatic and related interactions.

In addition, the isosteric heats of gas sorption (Q_{st}, Figure S26a), calculated *via* the common Clausius−Clapeyron approach using isotherm fits to a virial type equation, are consistent with this interpretation. The isosteric heats were also estimated using an integrated version of the Clausius−Clapeyron equation shown in Figure S26b,c.[41] The integrated form of the equation is equivalent to the differential form when employed over a small, effectively infinitesimal, temperature range. For the multitemperature measurements common in gas sorption, the integrated form has the advantage that multiple collinear points demonstrate that the inherent approximations are reasonable. This is especially important in the case of continuously flexible frameworks where a large change in structure or chemical environment makes Clausius−Clapeyron heats a reasonable estimate of the thermodynamics, but not a precise quantitative measure. The resulting temperature-dependent isosteric heats are reported and support the same conclusions. Note there is not a perfect way to extract sorption heats from isotherms in a continuously flexible material where Q_{st} will be everywhere loading and T dependent without performing calorimetry explicitly. This is also true for rigid frameworks if the sorption mechanism changes between isotherm temperatures. Nonetheless, the Clausius−Clapeyron Q_{st} values remain a valuable guide here. It is clear that specific sorbate−sorbent interactions are discernible from the neat isotherms, and this suggests their involvement in inducing sorbent conformational changes.

As shown in Figure S26a, the estimated initial Q_{st}^0 values of **NKU-FlexMOF-1a** are 32.2 kJ mol^{-1} for CO_2, 24.4 kJ mol^{-1} for CH_4, 33.5 kJ mol^{-1} for C_2H_6, 34.5 kJ mol^{-1} for C_2H_4, 52.5 kJ mol^{-1} for C_3H_8, 61.6 kJ mol^{-1} for C_3H_6, and 57.4 kJ mol^{-1} for C_4H_{10}. While the adsorption isotherms of N_2, CO_2, CH_4, C_2H_6, C_2H_4, C_3H_6, and C_4H_{10} are typical at 273 and 298 K, for C_3H_8 the behavior is anomalous. When the temperature is raised from 273 to 298 K, the overall C_3H_8 uptake increases as well; this phenomenon is rare in an exothermic physisorption process. Because entropic free energy contributions are favored at higher temperatures, sorption enthalpies must substantially increase with temperature. This too implies that collective structural changes take place in the porous material to account for the resulting stronger interactions.

Specifically, it is found that while the electrostatic environment remains remarkably similar for even different hydrocarbons (Table S8), the induced-fit nature of the compound provides repulsion and dispersion, aka van der Waals interactions, that lead to the observed distinct energetics. The structural changes are demonstrated to be small even in the fully loaded structures (Figure S45). However, the calculated energetics are still quite different, as shown in Table S7. The calculated energy differences are substantial and give rise to the observed separations and temperature enhanced sorption. The energetic differences necessarily arise largely from the repulsion and dispersion portions of the intermolecular potential energy. The repulsions are well thought of as exponentially distant dependent, and the dispersion attractions are a large inverse power of the distance. Thus, a subtle interplay between these functions gives rise to unique energetics for each sorbate and temperature. This situation is analogous to what is typically found in enzyme−substrate interactions with similar useful structure or function relationships.

To further explore this unusual behavior, the adsorption isotherms for C_3H_8 at different temperatures (258, 268, 273, 278, 288, 298, 308, 318, 328, 338, and 348 K) were measured. As shown in Figure 2a, in the range 258−318 K, the maximum saturated uptake amounts at 113 kPa gradually increase with increasing temperature. The sorbed amount reaches a maximum at about 318 K. At temperatures above 318 K, **NKU-FlexMOF-1a** exhibits typical adsorption behavior, where the sorption decreases as the temperatures increase (Figure 2b). From 258 to 318 K, the C_3H_8 uptake capacity in **NKU-FlexMOF-1a** increases considerably from 52.2 cm^3 g^{-1} (258 K) to 66.8 cm^3g^{-1} (318 K), a change of 14.6 cm^3 g^{-1}.

Considering the atypical sorption behavior of **NKU-FlexMOF-1a** for C_3H_8, the adsorption isotherms for C_2H_6, C_3H_6, and C_4H_{10} at different temperatures were also measured (Figure 2c−f). Interestingly, the sorption behaviors of C_2H_6 and C_3H_6 are similar to that of C_3H_8. Maximum saturated uptake amounts appear at 273 K for C_2H_6 and at 268 K for C_3H_6; subsequently, the uptake amounts gradually decrease with increasing temperature (Figure 2c−e). The magnitude of increasing sorption with temperature is different for C_2H_6, C_3H_6, and C_3H_8. For C_2H_6, when the temperature is increased from 248 to 273 K, the maximum saturated uptake increased by 6.8 cm^3 g^{-1}, from 65.6 cm^3 g^{-1} (248 K) to 72.4 cm^3 g^{-1} (273 K). Considering C_3H_6, the maximum saturated uptake amount increased by 2.0 cm^3 g^{-1}, from 71.7 to 73.7 cm^3 g^{-1} over a temperature range of 258−268 K. The resulting rates of change are 0.27, 0.20, 0.24 $cm^3{\cdot}g^{-1}{\cdot}K^{-1}$ for C_2H_6, C_3H_6, and C_3H_8, respectively.

Conversely, the adsorption isotherms for C_4H_{10} are typical with respect to uptake with temperature, but with an inflection clearly visible in the lower temperature isotherms (Figure 2f), reflecting the flexibility of the framework. The more typical uptake pattern indicates the sorbate−sorbent interactions are not strongly increasing with temperature; the larger size sorbate likely inhibits the ability to interact as effectively with the framework. Interestingly, the estimated isosteric heat still increases with loading on the basis of the differential, virial form analysis of the isotherms. Figure 2g shows the variation of saturated uptakes for C_2H_6, C_3H_6, C_3H_8, and C_4H_{10} at different temperatures highlighting the temperature enhanced sorption for C_2H_6, C_3H_6, and C_3H_8 within a particular temperature and pressure range.

Analysis of Framework Flexibility. The adsorption isotherms of **NKU-FlexMOF-1a** for N_2 and CO_2 at 77 and 195 K, respectively (Figures S6 and S16), exhibit a series of distinct steps at very low pressures from the framework flexibility. The structural changes resulting from guest loading conditions are challenging to characterize but can lead to an understanding of host−guest interactions and the corresponding framework flexibility.[42] Although some techniques, such as IR/Raman spectroscopy, NMR, and powder X-ray diffraction, have been used to probe the nature of sorbates in MOF

DOI: 10.1021/jacs.9b07807
J. Am. Chem. Soc. 2019, 141, 17703−17712

Table 1. Crystal Data Parameters for NKU-FlexMOF-1 at Different Conditions

	a (Å)	b (Å)	c (Å)	α (deg)	β (deg)	γ (deg)	V(Å^3)	T (K)
NKU-FlexMOF-1[a]	10.551	11.001	14.830	90	108.79	90	1629.7	298
NKU-FlexMOF-1a[b]	10.486	10.537	15.045	90	106.84	90	1591.2	298
NKU-FlexMOF-1a-N_2-a[c]	10.488	10.412	15.057	90	107.25	90	1571.3	100
NKU-FlexMOF-1a-N_2-b[d]	10.563	11.333	14.625	90	108.25	90	1662.7	100
NKU-FlexMOF-1a-CO_2	10.557	11.404	14.324	90	108.73	90	1633.1	195
NKU-FlexMOF-1a-C_2H_6	10.489	10.449	15.108	90	106.79	90	1585.2	298
NKU-FlexMOF-1a-C_3H_8	10.574	10.656	15.227	90	108.49	90	1627.2	298

[a]The compound contained solvent molecules DMF. [b]The compound removed solvent molecules DMF. [c]The compound contained one N_2 molecule in its asymmetric unit. [d]The compound contained three N_2 molecules in its asymmetric unit.

structures, the use of *in situ* single-crystal X-ray diffraction (SCXRD) is useful because it provides unequivocal structural information relating to different sorbent conformational states. Thus, single-crystal X-ray diffraction and *in situ* powder X-ray diffraction experiments were performed to characterize the flexibility of the framework **NKU-FlexMOF-1a** in the presence of sorbates.

Analyzing crystal data parameters (Table 1), the *b*-axis and *c*-axis of **NKU-FlexMOF-1a** change by −0.464 Å and +0.215 Å, respectively, compared with solvated **NKU-FlexMOF-1**, which demonstrates that the framework has shrunk after removing guest solvent DMF molecules. In addition, the crystal structures containing N_2 molecules at low or high pressures were obtained, respectively (the pressure of **NKU-FlexMOF-1a-N_2-a** < the pressure of **NKU-FlexMOF-1a-N_2-b**). With increasing N_2 pressure, the number of N_2 molecules in the channels increases and induces a swelling of the framework. This is evidenced by distinct changes of the *b*-axis and *c*-axis (+0.921 Å for *b*-axis and −0.432 Å for *c*-axis); the size and angles of the channel are also modified (Figure 3a). The sizes of the triangular channel changed from 8.24 × 9.54 × 8.74 Å^3 to 8.28 × 9.64 × 9.74 Å^3, and the angles of triangular channel changed from 96.6° × 89.0° × 92.2° to 92.6° × 89.5° × 91.3°. These changes are facilitated by the flexibility of the $FPBDC^{2-}$ ligand.

To better understand this behavior, the potential energy profile of H_2FPBDC at different conformations was calculated using density functional theory. With changing torsion angles between the pyridyl and phenyl rings, an energy barrier was located at the coplanar conformation. Its magnitude was found to be 1.7 kJ mol^{-1} between the two stable conformations (Figure S43). NJU-Bai7, using a similar ligand (5-(pyridin-3-yl) isophthalic acid) without an F-group, resulted in a structure analogous to that of **NKU-FlexMOF-1a**, but it is a N_2 adsorption isotherm that does not exhibit adsorption steps.[37] This suggests that the H_2FPBDC moiety, a short and flexible ligand, can be twisted to produce a framework change by overcoming a relatively low thermally accessible barrier *via* external stimuli.[43] The F-group on the ligand adds lability to the torsion, resulting in the stepwise N_2 adsorption behavior at 77 K. Thus, the functional group on the organic linker plays a significant role for the flexibility of the final MOF framework.[44] As a result, as shown in Figure S34, the dihedral angle between pyridyl and phenyl rings was enlarged by 3.489°, changed from 45.094 to 48.583°, when the number of N_2 molecules in the asymmetric unit increased. Further, the twist of the $FPBDC^{2-}$ ligand results in the angle between paddle-wheel SBUs and phenyl rings changing by −5.207 from 46.929 to 41.722°, and −0.996 from 21.482 to 20.486°.

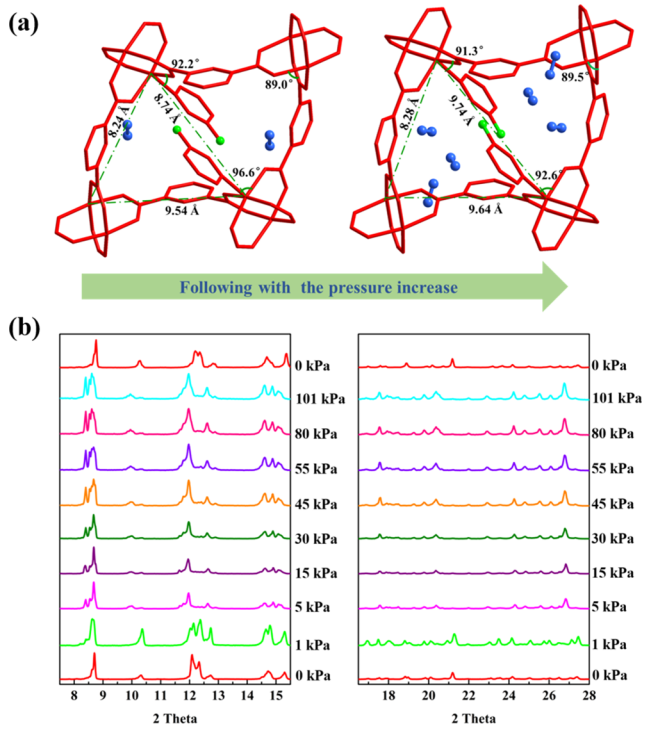

Figure 3. (a) With increasing N_2 pressure, the sizes and angles of triangular channels for **NKU-FlexMOF-1a-N_2-a** and **NKU-FlexMOF-1a-N_2-b** are shown from SCXRD. (b) *In situ* powder X-ray diffraction patterns are shown for **NKUFlexMOF-1a** at 83 K and variable N_2 pressures (as indicated) and are consistent with the structures seen in SCXRD.

Next, in order to understand the structural transformation in depth, *in situ* powder X-ray diffraction experiments were performed under various pressures of N_2 at 83 K. As shown in Figure 3b, from 0 to 5 kPa, there are substantial changes of the positions of the diffraction peaks, but between 5 and 101 kPa, there are only very small changes in position and minor changes to the intensities of some diffraction peaks. In the vacuum state, the PXRD pattern is the same as that of the sample at 0 kPa, which indicates that the expanded phase is reversibly converted back to the collapsed phase.

Further, the refinement of the *in situ* PXRD patterns of **NKU-FlexMOF-1a** at different N_2 pressures was performed. The results, as shown in Table S5, revealed that unit cell volume increases slowly followed by the increase of pressure, which shows the framework has the property of guest-induced flexibility. However, as shown in Figure S35, at 273 K the PXRD pattern does not exhibit obvious changes with an increase in N_2 pressure. Thus, the guest N_2 gas molecules at

DOI: 10.1021/jacs.9b07807
J. Am. Chem. Soc. 2019, 141, 17703−17712

low temperatures are sorbed with stronger framework interactions that trigger the ligand torsion leading to the structural changes reflected in the isotherms and a PXRD consistent with the low thermal barrier noted above with an energy corresponding to a temperature of about 200 K, as shown in Figure S43.

Guest-Induced Flexibility. In order to further explore the effect of CO_2 and hydrocarbon guest molecules on the flexible behavior of framework, the *in situ* powder X-ray diffraction patterns were measured at 298 K under different gas atmospheres (P = 100 kPa) corresponding to the asymptotic region of the gas isotherms where structural changes are complete for the sorbates considered. As shown in Figure 4

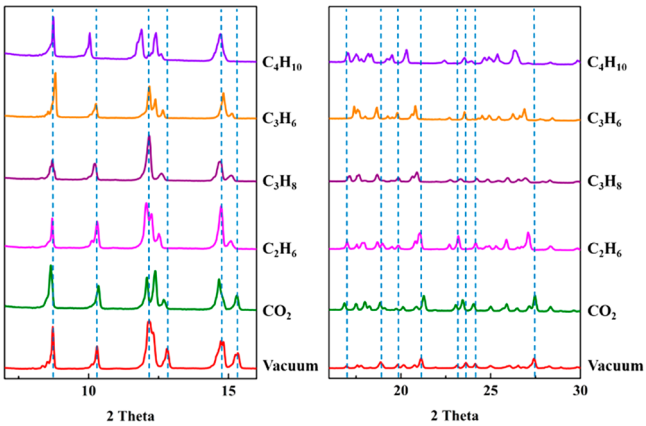

Figure 4. *In situ* powder X-ray diffraction patterns for **NKU-FlexMOF-1a** at room temperature and variable gas atmosphere (as indicated).

compared with **NKU-FlexMOF-1a** under a vacuum condition, the structural transformations induced by the guest molecules are evident. The changes are characteristic of the sorbate as reflected in the changes to the positions of the diffraction peaks in Figure 4 and correspond to distinct fits to each sorbate adapting to their mutual steric and attractive interactions. The diffraction peaks moving toward low angles indicate pore size increase, and the degrees of movement increase with the size of the guest molecules. Furthermore, considering a sample loaded with propane, the positions of the diffraction peaks exhibit mild shifts with varied temperature (Figure S40). This reflects that the framework loaded with propane changing with temperature.

In addition to *in situ* powder X-ray diffraction measurements, the crystal structures containing C_2H_6, C_3H_8, or CO_2 molecules were measured. When the crystal data of **NKU-FlexMOF-1a-C_2H_6**, **NKU-FlexMOF-1a-C_3H_8**, and **NKU-FlexMOF-1a-CO_2** are compared with the crystal data of **NKU-FlexMOF-1a** (Table 1), the unit parameters of **NKU-FlexMOF-1a-C_2H_6** are similar to the parameters of **NKU-FlexMOF-1a**, which coincides with *in situ* PXRD result that exhibits relatively small changes compared with those of other gas molecules. For **NKU-FlexMOF-1a-C_3H_8** and **NKU-FlexMOF-1a-CO_2**, their unit cell parameters show obvious changes. In the **NKU-FlexMOF-1a-C_3H_8** unit cell, all axes increase mildly and the β angle increases by 1.65°. When CO_2 molecules are entered into the channel of **NKU-FlexMOF-1a**, the unit cell parameter of the b-axis increases 0.9 Å and the c-axis decreases 0.7 Å. On the basis of above results, it can be confirmed that the different guest molecules lead to distinct conformational accommodations. At the room temperature, the sample was kept in equilibrium for long times in a C_3H_8 atmosphere, and the phase was assessed by using *in situ* powder X-ray diffraction; the sample was activated under a dynamic vacuum and the recovered phase was characterized. The experiments were recorded over four cycles, which exhibited good reversibility (Figure S41). Furthermore, the morphologies of **NKU-FlexMOF-1**, **NKU-FlexMOF-1a**, and the crystals after multiple cycles were compared by optical microscopy and scanning electron microscopy (SEM). As shown in Figure S42, the morphologies of the crystals after multiple cycles are retained.

These transformations reflect different intermolecular interactions between the guest molecules and the framework; a structure that responds distinctly, i.e., adapts subtly but meaningfully, to an array of chemically related species is a promising candidate for applications where physical sorbate–sorbent interactions seek to resolve similar molecules. This makes **NKU-FlexMOF-1** a desirable platform for hydrocarbon capture and separation, as the flexible framework response to sorption acts to distinguish between the chemical entities by more extensive interactions, e.g., through shape, charge, dispersion, or polarization, that are not possible in rigid sorbate–sorbent systems. In rigid platforms, only a small subset of physical and chemical interactions are sampled, as the sorbate is in contact with the sorbent for a restricted set of orientations and distances that cannot be mutually optimized, interacting with a rigid substrate. This limits the potential chemical resolution achievable through the rigid interactions, while a flexible material can capture the differences in structures through enhanced sampling of the interactions *via* the adaptable solid state structure as seen in **NKU-FlexMOF-1a**.

First-Principles Calculations on Framework Flexibility. In order to further explore the flexible nature of **NKU-FlexMOF-1a**, we compare the SCXRD structure of the as-synthesized **NKU-FlexMOF-1** with that of the activated sample **NKU-FlexMOF-1a**. Upon desolvation, the lattice unit cell shrinks slightly, mainly within the b–c plane. The overall unit cell volume decrease is quite small (only ~2.4%); however, the decrease in PLATON pore volume resulting from the structural change is significant at ~17% (0.291 *vs* 0.242 cc g^{-1}). This demonstrates how small structural accommodations can meaningfully adapt to sorbates.

To elucidate the mechanism of the structural flexibility, a detailed computational first-principles investigation was performed on the basis of dispersion-corrected density functional theory (DFT-D). The as-synthesized structure **NKU-FlexMOF-1**, using the coordinates with the solvent removed *in silico*, and the activated structure **NKU-FlexMOF-1a** were first fully geometry optimized. Then nudged elastic band calculations were performed to find a minimum energy path for the structural change between the two phases. An animation consisting of snapshots of the transformation clearly shows how the pore shrinks smoothly and continuously along the structural change coordinate (see Animation of transformations-1 Supporting Information).

In the **NKU-FlexMOF-1** structure, the $[Cu_2(COO)_4N_2]$ paddle-wheel, the linker phenyl ring, and the linker pyridine ring are relatively rigid, while the joints connecting these three types of rigid units are flexible, particularly in terms of the relative orientation of the linked units. These flexible

DOI: 10.1021/jacs.9b07807
J. Am. Chem. Soc. 2019, 141, 17703–17712

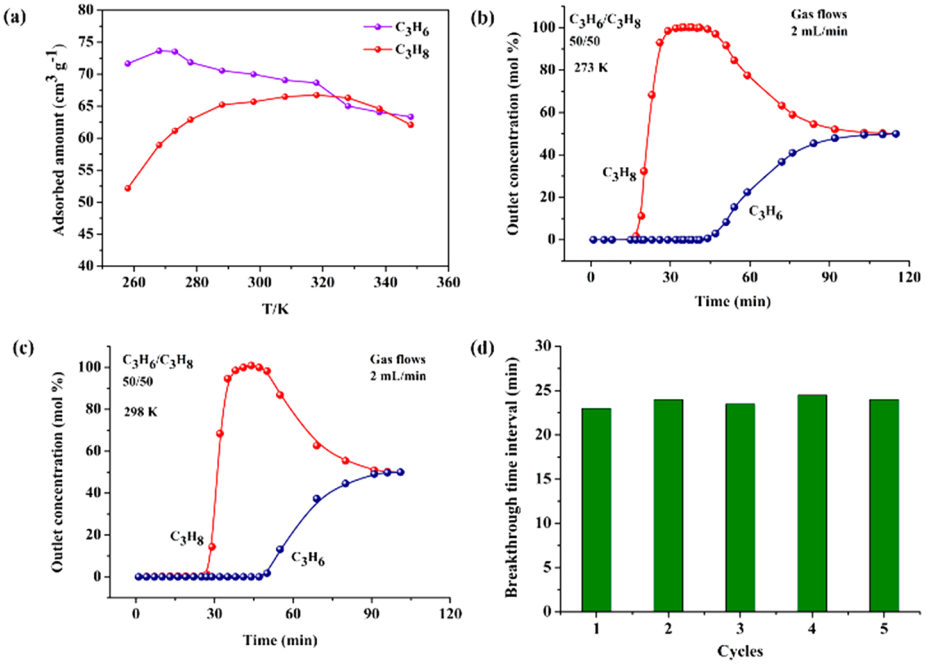

Figure 5. (a) Variation tendencies of saturated uptake amounts for C_3H_6 and C_3H_8 at different temperature (from 258 to 348 K at 1.1 bar). Experimental breakthrough curves for the C_3H_6/C_3H_8 (50/50, v/v) mixture through a bed of **NKU-FlexMOF-1a** material at (b) 273 and (c) 298 K. (d) Cyclic C_3H_6/C_3H_8 (50%/50%) separation on **NKU-FlexMOF-1a** material at 298 K and 1 bar.

coordination bonds are largely responsible for the flexibility of the **NKU-FlexMOF-1** framework.

Our lattice dynamics calculation on the activated structure **NKU-FlexMOF-1a** further shows that there are several low energy "soft" phonons, i.e., collective structural relaxation coordinates, resulting from these flexible coordination bonds (see Figure S44). Shown as an example in Supporting Information as Animation of transformations-2 is a phonon with ~4 meV energy (32 cm^{-1}), involving the rotation of the pyridyl rings. Upon guest inclusion, internal structural distortion takes place, mediated by the low frequency collective coordinates and may further couple with lattice distortions. Subtle conformational changes then mutually "optimize" the structure to interact effectively with different sorbates.

Breakthrough Experiments for Binary C_3H_6/C_3H_8 Mixtures. Remarkably, due to the unique adsorption behaviors for C_3H_6 and C_3H_8, as shown in Figure 5a, at a lower temperature range (258−273 K), the uptake amount of C_3H_6 is distinctly larger than that of C_3H_8, indicative of the C_3H_6/C_3H_8 selectivity in this range. This is confirmed *via* a breakthrough experiment for a C_3H_6/C_3H_8 (50/50, v/v) mixture on **NKU-FlexMOF-1a** material at 273 and 298 K (Figure S46), to check its actual separation ability for the gas mixture. As shown in Figure 5b,c C_3H_8 first broke through the adsorption bed and yielded a high purity gas (>99.99%), whereas after a certain time C_3H_6 slowly eluted. The long breakthrough time interval between C_3H_6 and C_3H_8 suggests that **NKU-FlexMOF-1a** material is effective for practical C_3H_6/C_3H_8 separation as was suggested by the thermodynamic and structural results above. According to the breakthrough experiment, as shown in Table S6 and Figure S23, the calculated adsorption capacity of C_3H_6 is 1.96 mmol g^{-1} and the selectivity is 2.31 at 1 bar at 298 K, and the adsorption capacity and selectivity are 2.13 mmol g^{-1} and 2.66 at 1 bar at 273 K, respectively. The calculated adsorption capacity of C_3H_8 at 298 K is higher than that at 273 K, which is in line with the adsorption results. In addition, after the breakthrough experiment, the purity of desorbed propylene is 85.2%, as shown in Figure S24, which was consistent with the calculated selectivity. Afterward, cycling breakthrough experiments on **NKU-FlexMOF-1a** material were carried out under the same conditions. The breakthrough time intervals for C_3H_6/C_3H_8 mixtures in five cycles (Figure 5d) are close (~24 min), showing that this material has a good regenerability. Note the difference of adsorption capacity is the largest at 258 K, but our current laboratory setup is unable to perform the analogous colder experiments. Then we carried out breakthrough simulations for a C_3H_6/C_3H_8 (50/50, v/v) mixture, in a fixed bed to demonstrate the feasibility of separation of propylene and propane in a pressure swing adsorption operation at 258 K (Figure S25). The simulations also demonstrate the **NKU-FlexMOF-1a** is of potential use for this challenging separation of C_3H_6/C_3H_8 mixtures.

Analysis of Gas Adsorption and Separation Behavior. Flexible MOFs have transformable frameworks that are able to reversibly respond to external stimuli such as temperature, pressure, light, electric/magnetic fields, or the presence of particular species. Understanding how these materials change when perturbed will have applications in the development of smart materials and superior separations. Ideally, identification of extant and design of aspirational materials with adaptive properties is possible given a detailed understanding of relevant intermolecular interactions.

Here, a flexible microporous MOF showing inversely enhanced adsorption behavior for C_2H_6, C_3H_6, and C_3H_8 in a defined temperature and pressure range is presented. The increase in sorption with temperature is attributed to the dynamic behavior of **NKU-FlexMOF-1a** where guest molecules subtly interacting with an adaptive framework lead to an induced-fit specific to each sorbate. Notably, the material geometry and chemical environment is little changed between sorbates and the energetic differences are attributable to the

DOI: 10.1021/jacs.9b07807
J. Am. Chem. Soc. 2019, 141, 17703−17712

detailed changes in the van der Waals, aka repulsion and dispersion, interactions similar to enzyme−substrate interaction mechanisms. Further, to confirm that equilibrium phenomena is not the determining factor, the C_3H_8 isotherm at 258 and 298 K was obtained with long equilibration intervals between two points (at least 124 min). As shown in Figure S15, the adsorption amount at 298 K is consistently larger than that at 258 K, which is consistent with the trend reported in the pristine measurement. These results indicate that the inversely increased gas uptake at higher temperature should be due to the structure change of the **NKU-FlexMOF-1a** at different temperatures instead of the different diffusion resistances.

To understand why it is requisite that the framework is adaptive in response to sorbate contact, examine the thermodynamics of sorption. Because the magnitude of thermodynamic sorption at constant pressure (P) and temperature (T) is governed by the Gibbs free energy $G = H - TS$, an increase in temperature will necessarily lead to decreased sorption if the material can be considered a rigid framework. Consider the entropy of the sorbate is decreased with substantial interaction with a rigid or flexible framework as the conformational space it can explore is restricted; for example, the rotations are hindered, and the relatively large translational entropy contribution is greatly diminished. Thus, the entropy change upon "binding" is negative. Because the intermolecular interactions are temperature independent (i.e., the potential energy function is not T dependent), the only way for the free energy to decrease is for the enthalpy to sharply decrease with increasing temperature.

Given the enthalpy, $H = E + PV$, there is no significant differential contribution from the PV term upon contact, and thus the interaction energy must substantially decrease as T increases. This can only happen as a result of the material changing its conformation to produce more stable interactions with sorbates, implying closer contacts with more favorable molecular interactions than were present in the lower T structure. To this point, consider that a single structure will have larger amplitude thermal motions with increasing temperature that would tend to decrease the sorbate−sorbent system enthalpy, and only a mutually beneficial structural change can explain the observed increase in sorption that is referred to herein as an induced-fit mechanism. This is what is observed in the case of **NKU-FlexMOF-1a**, a flexible MOF that has adaptive conformational transformations in response to contact with the different sorbate molecules tested. Many of them show atypical increases in sorption with temperature, all of which have isotherms characteristic of material structural changes in response to sorption and similar structures for comparable loadings.

The nature of the conformational changes observed is guest specific and related to the detailed sorbate−sorbent interactions in the adaptive micropores of **NKU-FlexMOF-1a**. The maximum saturated uptake amounts of C_2H_6, C_3H_6, and C_3H_8 gradually increase, which is an atypical behavior compared with conventional physical adsorption. CO_2, N_2, and C_4H_{10} also induce structural changes but show typical diminished sorption as temperature is increased. Understanding the detailed nature of the different behaviors requires further investigation and careful molecular modeling. Nonetheless, the distinct temperature dependence of the sorbent enthalpies and the material stability make **NKU-FlexMOF-1a** an exciting candidate for hydrocarbon and potentially other small molecule separations *via* the induced-fit mechanism.

Further, on the basis of the observed adsorption behavior at the different temperatures considered, there is a useful difference in adsorption capacity between C_3H_6 and C_3H_8 that can be employed for selective separation of C_3H_6/C_3H_8. Along this line, the breakthrough experiment and simulation both demonstrate **NKU-FlexMOF-1a** is of potential use for this challenging separation of C_3H_6/C_3H_8 mixtures.

To better understand the separation mechanism, the saturated crystal structures, reported here, of C_3H_8 and C_2H_6 were taken and optimized using dispersion-corrected periodic DFT calculations in the program CP2K.[45] C_2H_6 calculations serve as a point of calibration and reference in interpreting the results. Next, the C_3H_8 molecules were mutated to C_3H_6 *in silico* and optimizations were performed with a resulting 0.204 Å RMSD between the resulting framework coordinates. The resulting structures are shown superimposed (Figure S45) and have analogous structures that imply separation mechanisms that are similarly mediated by different detailed energetics *via* van der Waals repulsions and attractions, consistent with the induced-fit mechanism.

The nature of the sorption is similar; the separation chemistry and surface areas will be comparable for the separations considered. This was further confirmed by examining derived partial charges for saturated structures that demonstrate the commensurate chemistry evidenced by the highly similar electrostatic environment (Table S8). The energy per sorbate was also calculated in the loaded, effectively zero temperature configuration, and calculations consistently show the sorption energy averaged over fully loaded configurations with $E(C_3H_8) \approx E(C_3H_6) \gg E(C_2H_6)$; values are presented in Table S7. While the double bonded C_3H_6 will clearly have enhanced electrostatic interactions, the conformational adaptation leads to enough increase in van der Waals energies that both propane and propene are substantially higher in binding energy than ethane that are similarly bound.

CONCLUSION

In summary, we report a flexible microporous MOF (**NKU-FlexMOF-1**), which exhibits sorbate induced-fit dynamic behavior. On the basis of the behavior, sorption of C_2H_6, C_3H_6, and C_3H_8 in **NKU-FlexMOF-1a** increases with rising temperature over a practically useful temperature and pressure range. Then the difference in adsorption capacity between C_3H_6 and C_3H_8 can induce the selective separation of C_3H_6/C_3H_8. Therefore, this work provides not only a new flexible MOF with distinct and useful adsorption behaviors for C_2H_6, C_3H_6, and C_3H_8 but also a design strategy of seeking and constructing flexible, induced-fit MOFs with flexible ligand motions; the material responds distinctly to sorbates of interest for gas capture and separation, exploiting the extreme sensitivity of repulsion and dispersion interactions to small changes in distance. Materials with adaptive structural characteristics and tunable host−guest interactions as a function of both sorbate and temperature have a much wider range of utility than rigid materials. The induced-fit mechanism revealed in this study provides new directions for the design of flexible MOFs for the development of adsorption-based separation and capture technologies.

DOI: 10.1021/jacs.9b07807
J. Am. Chem. Soc. 2019, 141, 17703−17712

■ ASSOCIATED CONTENT

Supporting Information

The Supporting Information is available free of charge on the ACS Publications website at DOI: 10.1021/jacs.9b07807.

NKU-FlexMOF-1 checkCIF/PLATON reports and CIF files (ZIP)

Materials and measurements, details of syntheses, gas sorption data, calculations on framework flexibility, and gas adsorption, tables of crystal data and structure refinement parameters, Cu^{2+} in aqueous solutions, unit cell parameters, PXRD patterns, binding energies, and average partial charges, figures of TG curves, VT-PXRD patterns, images of crystals, adsorption isotherms, adsorption points, calculated selectivity, components of desorbed mixtures, breakthrough simulations, isosteric heats, details of virial equations, structure analysis, X-ray diffraction patterns, torsional landscape, DFT-D calculated phonon density of states, and schematic diagram of device of breakthrough experiments (PDF)

Animation of transformations-1 (GIF)

Animation of transformations-2 (GIF)

■ AUTHOR INFORMATION

Corresponding Authors

*tlhu@nankai.edu.cn

*buxh@nankai.edu.cn

ORCID

Wei Zhou: 0000-0002-5461-3617

Rajamani Krishna: 0000-0002-4784-8530

Ze Chang: 0000-0002-3865-2165

Wei Li: 0000-0002-5277-6850

Tong-Liang Hu: 0000-0001-9619-9867

Xian-He Bu: 0000-0002-2646-7974

Notes

The authors declare no competing financial interest.

■ ACKNOWLEDGMENTS

This work was supported by the NSFC (21673120, 21606163, 21531005, and 91856124). We thank the staffs from the BL17B beamline of the National Facility for Protein Science in Shanghai (NFPS) at the Shanghai Synchrotron Radiation Facility for assistance during data collection. B.S. and D.F. acknowledge the National Science Foundation (Award No. DMR 1607989), including support from the Major Research Instrumentation Program (Award No. CHE 1531590). B.S. and D.F. acknowledge computational resources made available by a XSEDE Grant (No. TG DMR090028) and by Research Computing at the University of South Florida. The authors thank Prof. Banglin Chen (University of Texas at San Antonio, Texas) for discussions and help.

■ REFERENCES

(1) Kim, H.; Yang, S.; Rao, S. R.; Narayanan, S.; Kapustin, E. A.; Furukawa, H.; Umans, A. S.; Yaghi, O. M.; Wang, E. N. Water harvesting from air with metal-organic frameworks powered by natural sunlight. *Science* **2017**, *356* (6336), 430−434.

(2) Liao, P. Q.; Huang, N. Y.; Zhang, W. X.; Zhang, J. P.; Chen, X. M. Controlling guest conformation for efficient purification of butadiene. *Science* **2017**, *356* (6343), 1193−1196.

(3) Howarth, A. J.; Liu, Y.; Li, P.; Li, Z.; Wang, T. C.; Hupp, J. T.; Farha, O. K. Chemical, thermal and mechanical stabilities of metal-organic frameworks. *Nat. Rev. Mater.* **2016**, *1*, 15018.

(4) Cadiau, A.; Adil, K.; Bhatt, P. M.; Belmabkhout, Y.; Eddaoudi, M. A metal-organic framework-based splitter for separating propylene from propane. *Science* **2016**, *353* (6295), 137−140.

(5) Lu, W.; Verdegaal, W. M.; Yu, J.; Balbuena, P. B.; Jeong, H.; Zhou, H. C. Building multiple adsorption sites in porous polymer networks for carbon capture applications. *Energy Environ. Sci.* **2013**, *6* (12), 3559−3564.

(6) Bachman, J. E.; Smith, Z. P.; Li, T.; Xu, T.; Long, J. R. Enhanced ethylene separation and plasticization resistance in polymer membranes incorporating metal-organic framework nanocrystals. *Nat. Mater.* **2016**, *15*, 845−851.

(7) Yan, Y.; Kolokolov, D. I.; da Silva, I.; Stepanov, A. G.; Blake, A. J.; Dailly, A.; Manuel, P.; Tang, C. C.; Yang, S.; Schröder, M. Porous metal-organic polyhedral frameworks with optimal molecular dynamics and pore geometry for methane storage. *J. Am. Chem. Soc.* **2017**, *139* (38), 13349−13360.

(8) Ji, P. F.; Solomon, J. B.; Lin, Z.; Johnson, A.; Jordan, R. F.; Lin, W. Transformation of metal-organic framework secondary building units into hexanuclear Zr-alkyl catalysts for ethylene polymerization. *J. Am. Chem. Soc.* **2017**, *139* (33), 11325−11328.

(9) Li, B.; Dong, X.; Wang, H.; Ma, D.; Tan, K.; Jensen, S.; Deibert, B. J.; Butler, J.; Cure, J.; Shi, Z.; Thonhauser, T.; Chabal, Y. J.; Han, Y.; Li, J. Capture of organic iodides from nuclear waste by metal-organic framework-based molecular traps. *Nat. Commun.* **2017**, *8*, 485.

(10) Chang, Z.; Yang, D. H.; Xu, J.; Hu, T. L.; Bu, X. H. Flexible metal-organic frameworks: Recent advances and potential applications. *Adv. Mater.* **2015**, *27* (36), 5432−5441.

(11) Schneemann, A.; Bon, V.; Schwedler, I.; Senkovska, I.; Kaskel, S.; Fischer, R. A. Flexible metal-organic frameworks. *Chem. Soc. Rev.* **2014**, *43* (16), 6062−6096.

(12) Zhu, A.-X.; Yang, Q.-Y.; Kumar, A.; Crowley, C.; Mukherjee, S.; Chen, K.-J.; Wang, S.-Q.; O'Nolan, D.; Shivanna, M.; Zaworotko, M. J. Coordination network that reversibly switches between two nonporous polymorphs and a high surface area porous phase. *J. Am. Chem. Soc.* **2018**, *140* (46), 15572−15576.

(13) Carrington, E. J.; McAnally, C. A.; Fletcher, A. J.; Thompson, S. P.; Warren, M.; Brammer, L. Solvent-switchable continuous-breathing behavior in a diamondoid metal-organic framework and its influence on CO_2 versus CH_4 selectivity. *Nat. Chem.* **2017**, *9*, 882−889.

(14) Pang, J. D.; Yuan, S.; Du, D.; Lollar, C.; Zhang, L.; Wu, M.; Yuan, D.; Zhou, H. C.; Hong, M. Flexible zirconium MOFs as bromine-nanocontainers for bromination reactions under ambient conditions. *Angew. Chem., Int. Ed.* **2017**, *56* (46), 14622−14626.

(15) Sakata, Y.; Furukawa, S.; Kondo, M.; Hirai, K.; Horike, N.; Takashima, Y.; Uehara, H.; Louvain, N.; Meilikhov, M.; Tsuruoka, T.; Isoda, S.; Kosaka, W.; Sakata, O.; Kitagawa, S. Shape-memory nanopores induced in coordination frameworks by crystal downsizing. *Science* **2013**, *339* (6116), 193−196.

(16) Salles, F.; Maurin, G.; Serre, C.; Llewellyn, P. L.; Knöfel, C.; Choi, H. J.; Filinchuk, Y.; Oliviero, L.; Vimont, A.; Long, J. R.; Férey, G. Multistep N_2 breathing in the metal-organic framework Co (1,4-benzenedipy- razolate). *J. Am. Chem. Soc.* **2010**, *132* (39), 13782−13788.

(17) Yang, W.; Davies, A. J.; Lin, X.; Suyetin, M.; Matsuda, R.; Blake, A. J.; Wilson, C.; Lewis, W.; Parker, J. E.; Tang, C. C.; George, M. W.; Hubberstey, P.; Kitagawa, S.; Sakamoto, H.; Bichoutskaia, E.; Champness, N. R.; Yang, S.; Schröder, M. Selective CO_2 uptake and inverse CO_2/C_2H_2 selectivity in a dynamic bifunctional metal-organic framework. *Chem. Sci.* **2012**, *3* (10), 2993−2999.

(18) Takashima, Y.; Martínez, V. M.; Furukawa, S.; Kondo, M.; Shimomura, S.; Uehara, H.; Nakahama, M.; Sugimoto, K.; Kitagawa, S. Molecular decoding using luminescence from an entangled porous framework. *Nat. Commun.* **2011**, *2*, 168.

(19) Yanai, N.; Kitayama, K.; Hijikata, Y.; Sato, H.; Matsuda, R.; Kubota, Y.; Takata, M.; Mizuno, M.; Uemura, T.; Kitagawa, S. Gas detection by structural variations of fluorescent guest molecules in a flexible porous coordination polymer. *Nat. Mater.* **2011**, *10*, 787−793.

(20) Yang, F.; Xu, G.; Dou, Y.; Wang, B.; Zhang, H.; Wu, H.; Zhou, W.; Li, J. R.; Chen, B. A flexible metal-organic framework with a high density of sulfonic acid sites for proton conduction. *Nat. Energy* **2017**, *2*, 877−883.
(21) Chen, Q.; Chang, Z.; Song, W. C.; Song, H.; Song, H. B.; Hu, T. L.; Bu, X. H. A controllable gate effect in Cobalt(II) organic frameworks by reversible structure transformations. *Angew. Chem., Int. Ed.* **2013**, *52* (44), 11550−11553.
(22) Wang, Y.; Huang, N. Y.; Zhang, X. W.; He, H.; Huang, R. K.; Ye, Z. M.; Li, Y.; Zhou, D. D.; Liao, P. Q.; Chen, X. M.; Zhang, J. P. Selective aerobic oxidation of a metal-organic framework boosts thermodynamic and kinetic propylene/propane selectivity. *Angew. Chem., Int. Ed.* **2019**, *58* (23), 7692−7696.
(23) Férey, G.; Serre, C. Large breathing effects in three-dimensional porous hybrid matter: Facts, analyses, rules and consequences. *Chem. Soc. Rev.* **2009**, *38* (5), 1380−1399.
(24) Coudert, F.-X.; Boutin, A.; Jeffroy, M.; Mellot-Draznieks, C.; Fuchs, A. H. Thermodynamic methods and models to study flexible metal-organic frameworks. *ChemPhysChem* **2011**, *12* (2), 247−258.
(25) Horike, S.; Shimomura, S.; Kitagawa, S. Soft porous crystals. *Nat. Chem.* **2009**, *1*, 695−704.
(26) Le Ouay, B.; Kitagawa, S.; Uemura, T. Opening of an accessible microporosity in an otherwise nonporous metal-organic framework by polymeric guests. *J. Am. Chem. Soc.* **2017**, *139* (23), 7886−7892.
(27) Zornoza, B.; Martinez-Joaristi, A.; Serra-Crespo, P.; Tellez, C.; Coronas, J.; Gascon, J.; Kapteijn, F. Functionalized flexible MOFs as fillers in mixed matrix membranes for highly selective separation of CO_2 from CH_4 at elevated pressures. *Chem. Commun.* **2011**, *47* (33), 9522−9524.
(28) Rodenas, T.; van Dalen, M.; Garcia-Perez, E.; Serra-Crespo, P.; Zornoza, B.; Kapteijn, F.; Gascon, J. Visualizing MOF mixed matrix membranes at the nanoscale: Towards structure-performance relationships in CO_2/CH_4 separation over NH_2-MIL-53(Al)@PI. *Adv. Funct. Mater.* **2014**, *24* (2), 249−256.
(29) Sato, H.; Kosaka, W.; Matsuda, R.; Hori, A.; Hijikata, Y.; Belosludov, V. R.; Sakaki, S.; Takata, M.; Kitagawa, S. Self-accelerating CO sorption in a soft nanoporous crystal. *Science* **2014**, *343* (6167), 167−170.
(30) Liao, P. Q.; Zhang, W. X.; Zhang, J. P.; Chen, X. M. Efficient purification of ethene by an ethane-trapping metal-organic framework. *Nat. Commun.* **2015**, *6*, 8697.
(31) Hu, T. L.; Wang, H.; Li, B.; Krishna, R.; Wu, H.; Zhou, W.; Zhao, Y.; Han, Y.; Wang, X.; Zhu, W.; Yao, Z.; Xiang, S.; Chen, B. Microporous metal-organic framework with dual functionalities for highly efficient removal of acetylene from ethylene/acetylene mixtures. *Nat. Commun.* **2015**, *6*, 7328.
(32) Li, L.; Lin, R. B.; Krishna, R.; Wang, X.; Li, B.; Wu, H.; Li, J.; Zhou, W.; Chen, B. Flexible-robust metal-organic framework for efficient removal of propyne from propylene. *J. Am. Chem. Soc.* **2017**, *139* (23), 7733−7736.
(33) Sen, S.; Hosono, N.; Zheng, J. J.; Kusaka, S.; Matsuda, R.; Sakaki, S.; Kitagawa, S. Cooperative bond scission in a soft porous crystal enables discriminatory gate opening for ethylene over ethane. *J. Am. Chem. Soc.* **2017**, *139* (50), 18313−18321.
(34) Cui, X.; Chen, K.; Xing, H.; Yang, Q.; Krishna, R.; Bao, Z.; Wu, H.; Zhou, W.; Dong, X.; Han, Y.; Li, B.; Ren, Q.; Zaworotko, J. M.; Chen, B. Pore chemistry and size control in hybrid porous materials for acetylene capture from ethylene. *Science* **2016**, *353* (6295), 141−144.
(35) Li, B.; Cui, X.; O'Nolan, D.; Wen, H. M.; Jiang, M.; Krishna, R.; Wu, H.; Lin, R. B.; Chen, Y. S.; Yuan, D.; Xing, H.; Zhou, W.; Ren, Q.; Qian, G.; Zaworotko, J. M.; Chen, B. An ideal molecular sieve for acetylene removal from ethylene with record selectivity and productivity. *Adv. Mater.* **2017**, *29* (47), 1704210.
(36) Yang, Q. Y.; Lama, P.; Sen, S.; Lusi, M.; Chen, K. J.; Gao, W. Y.; Shivanna, M.; Pham, T.; Hosono, N.; Kusaka, S.; Perry, J. J.; Ma, S.; Space, B.; Barbour, L. J.; Kitagawa, S.; Zaworotko, M. J. Reversible switching between highly porous and nonporous phases of an interpenetrated diamondoid coordination network that exhibits gate-opening at methane storage pressures. *Angew. Chem., Int. Ed.* **2018**, *57* (20), 5684−5689.
(37) Du, L.; Lu, Z.; Zheng, K.; Wang, J.; Zheng, X.; Pan, Y.; You, X.; Bai, J. Fine-tuning pore size by shifting coordination sites of ligands and surface polarization of metal-organic frameworks to sharply enhance the selectivity for CO_2. *J. Am. Chem. Soc.* **2013**, *135* (2), 562−565.
(38) Mason, J. A.; Oktawiec, J.; Taylor, M. K.; Hudson, M. R.; Rodriguez, J.; Bachman, J. E.; Gonzalez, M. I.; Cervellino, A.; Guagliardi, A.; Brown, C. M.; Llewellyn, P. L.; Masciocchi, N.; Long, J. R. Methane storage in flexible metal-organic frameworks with intrinsic thermal management. *Nature* **2015**, *527*, 357−361.
(39) Taylor, M. K.; Runcevski, T.; Oktawiec, J.; Bachman, J. E.; Siegelman, R. L.; Jiang, H.; Mason, J. A.; Tarver, J. D.; Long, J. R. Near-perfect CO_2/CH_4 selectivity achieved through reversible guest templating in the flexible metal−organic framework. *J. Am. Chem. Soc.* **2018**, *140* (32), 10324−10331.
(40) Li, J. R.; Kuppler, R. J.; Zhou, H. C. Selective gas adsorption and separation in metal-organic frameworks. *Chem. Soc. Rev.* **2009**, *38* (5), 1477−1504.
(41) Bao, Z.; Yu, L.; Ren, Q.; Lu, X.; Deng, S. G. Adsorption of CO_2 and CH_4 on a magnesium-based metal organic framework. *J. Colloid Interface Sci.* **2011**, *353* (2), 549−556.
(42) Lama, P.; Aggarwal, H.; Bezuidenhout, C. X.; Barbour, L. J. Giant hysteretic sorption of CO_2: In situ crystallographic visualization of guest binding within a breathing framework at 298 K. *Angew. Chem., Int. Ed.* **2016**, *55* (42), 13271−13275.
(43) Zhou, H. L.; Lin, R. B.; He, C. T.; Zhang, Y. B.; Feng, N.; Wang, Q.; Deng, F.; Zhang, J. P.; Chen, X. M. Direct visualization of a guest-triggered crystal deformation based on a flexible ultramicroporousb framework. *Nat. Commun.* **2013**, *4*, 2534.
(44) Taylor, M. K.; Runčevski, T.; Oktawiec, J.; Gonzalez, I. M.; Siegelman, L. R.; Mason, A. J.; Ye, J.; Brown, M. C.; Long, R. J. Tuning the adsorption-induced phase change in the flexible metal-organic framework Co(bdp). *J. Am. Chem. Soc.* **2016**, *138* (45), 15019−15026.
(45) Hutter, J.; Iannuzzi, M.; Schiffmann, F.; VandeVondele, J. CP2K: atomistic simulations of condensed matter systems. *WIREs Comput. Mol. Sci.* **2014**, *4* (1), 15−25.

DOI: 10.1021/jacs.9b07807
J. Am. Chem. Soc. 2019, 141, 17703−17712

Supplementary Information

Enhanced Gas Uptake in a Microporous Metal-Organic Framework *via* a Sorbate Induced-Fit Mechanism

Mei-Hui Yu,[†] Brian Space,[§] Douglas Franz,[§] Wei Zhou,[‖] Chaohui He,[⊥] Libo Li,[⊥] Rajamani Krishna,[#] Ze Chang,[†] Wei Li,[†] Tong-Liang Hu*,[†] and Xian-He Bu*,[†,‡]

[†]School of Materials Science and Engineering, National Institute for Advanced Materials, Nankai University, Tianjin 300350, China

[‡]State Key Laboratory of Elemento-Organic Chemistry, and Collaborative Innovation Center of Chemical Science and Engineering, Nankai University, Tianjin 300071, China

[§]Department of Chemistry, University of South Florida, 4202 East Fowler Avenue, Tampa, Florida 33620, United States

[‖]NIST Center for Neutron Research, National Institute of Standards and Technology, Gaithersburg, Maryland 20899-6102, United States

[⊥]Shanxi Key Laboratory of Gas Energy Efficient and Clean Utilization, College of Chemistry and Chemical Engineering, Taiyuan University of Technology, Taiyuan, 030024, Shanxi, China

[#]Van ‘t Hoff Institute for Molecular Sciences, University of Amsterdam, Science Park 904, Amsterdam 1098 XH, The Netherlands

Methods

Materials and measurements. Commercially available reagents were purchased in high purity and used without further purification. Thermogravimetric analysis (TGA) was carried out on a Rigaku standard TG-DTA analyzer between room temperature and 800 ℃ with a heating rate of 10 ℃ min^{-1}, using an empty Al_2O_3 crucible as reference. Elemental analysis (C, H, and N) was performed on a vario EL cube elemental analyzer. Powder X-ray diffraction (PXRD) was measured on a Rigaku Miniflex 600 at 40 kV and 15 mA with a scan rate of 3.0 deg min^{-1}, recorded in the range $3°\leq 2\theta \leq 50°$, using Cu- Kα radiation. *In situ* powder X-ray diffraction was measured on a Rigaku Smart Lab at 40 kV and 40 mA with an Anton Paar TTK 600 accessory.

Synthesis of NKU-FlexMOF-1. A mixture of $CuCl_2$ $2H_2O$ (6.8 mg, 0.04 mmol) and ligand H_2FPBDC (10.4 mg, 0.04 mmol) was dispersed into 2 mL mixed solvent (DMF/MeOH, 3/1, v/v) in a 10 mL screw-capped vial. To this was added 0.01 mL of concentrated HNO_3 with stirring. The resulting solution was heated to 80 ℃ for 48 h. After cooling to room temperature, blue block crystals were obtained by filtration and washed with DMF several times. Then, the crystals were transferred and stored in fresh DMF. The yield was about 70% based on the metal. Elem anal (%). Calcd for **NKU-FlexMOF-1** ($C_{16}H_{13}CuFN_2O_5$): C, 48.51; H, 3.28; N, 7.07. Found: C, 48.57; H, 3.20; N, 7.12.

Single-crystal X-ray crystallography. The **NKU-FlexMOF-1** diffraction data were collected on Rigaku SCX-mini diffractometer with Mo-Kα radiation (λ= 0.71073 Å). The **NKU-FlexMOF-1a-N_2-a** diffraction data were collected on BL17B beamline of National Facitity for Protein Science in Shanghai (NFPS). The other diffraction data were collected on a Rigaku XtaLAB Pro MM007HF DW diffractometer at different temperature with Cu-Kα radiation (λ= 1.54184 Å) by scan mode. The structure was solved by direct methods using SHELXTL program and refined by full-matrix least squares on F^2 using SHELXL. Metal atoms in **NKU-FlexMOF-1** were located from

the *E*-maps and other non-hydrogen atoms were subsequently located in successive difference Fourier synthesis and refined anisotropically. Crystal data for all the compounds were summarized in Supplementary Tables 1-3. And all structures containing gas molecules were measured by tube-sealing technique. The X-ray crystallographic coordinates for structures reported in this article have been deposited at the Cambridge Crystallographic Data Centre (CCDC), under deposition nos. CCDC: 1840016 (**NKU-FlexMOF-1**), 1840017 (**NKU-FlexMOF-1a**), 1840018 (**NKU-FlexMOF-1a-C_2H_6**), 1840019 (**NKU-FlexMOF-1a-C_3H_8**), 1840020 (**NKU-FlexMOF-1a-CO_2**), 1840021 (**NKU-FLEXMOF-1a-N_2-a**) and 1840022 (**NKU-FLEXMOF-1a-N_2-b**). These data can be obtained free of charge from The Cambridge Crystallographic Data Centre via www.ccdc.cam.ac.uk/data_request/cif.

Gas sorption studies. Gas adsorption isotherms for pressures in the range of 0–1.1 bar were measured using a Micrometrics ASAP 2020M volumetric gas adsorption analyzer. A sample of activated **NKU-FlexMOF-1a** (about 200 mg) was used for the sorption measurement and was maintained at 77 K with liquid nitrogen, and the bath temperatures of 248-358 K were precisely controlled with a LAUDR RP890 recirculating control system containing a mixture of ethylene glycol and water or ethyl alcohol.

Breakthrough experiment. The breakthrough separation apparatus consisted of two fixed-bed stainless steel reactors. One reactor was loaded with MOF powder (1.4682 g), while the other reactor was used as a blank control group to stabilize the gas flow. The horizontal reactors were placed in a temperature controlled environment, maintained at 273 K / 298 K. The flow rates of all gases mixtures were regulated by mass flow controllers without carrier gas, and the effluent gas stream from the column is monitored by a gas chromatography (TCD-Thermal Conductivity Detector, detection limit 0.1%). Prior to the each breakthrough experiment, we regenerated the sample by flushing the adsorption bed with helium gas (20 ml/min) for 30 min at 273 K / 298 K.

First-principles calculations on framework flexibility. First-principles density functional theory calculations were performed using the Quantum-Espresso package.[1] A semiempirical addition of dispersive forces to conventional DFT was included in the calculation to account for van der Waals interactions.[2] We used Vanderbilt-type ultrasoft pseudopotentials and generalized gradient approximation (GGA) with a Perdew−Burke−Ernzerhof (PBE) exchange correlation. A cutoff energy of 544 eV and a 4 × 4 × 4 k-point mesh (generated using the Monkhosrt-Pack scheme) were found to be enough for the total energy to converge within 0.01 meV/atom. Spin polarization was applied in all calculations, and the two Cu centers in the paddle wheel are coupled antiferromagnetically in the lowest energy state. To study the structural flexibility, full structural relaxations were first performed on the as-synthesized **NKU-FlexMOF-1** phase and the desolvated **NKU-FlexMOF-1a** phase. Then, nudged elastic band calculations were performed to find the minimum energy path of the structural transition between the two phases. Lattice dynamics phonon calculations were performed on the DFT-optimized **NKU-FlexMOF-1a** structure, using the supercell method (2×2×2 cell size) with finite displacements.[3] The supercell method involves perturbing the positions of the atoms slightly (0.02 Å displacement was used in this work) and calculating the reaction forces. Force constant matrix is then constructed, and through Fourier transform, dynamic matrix is derived and phonon frequencies are obtained.

The energy profile of H_2FPBDC was calculated using DFT via the Gaussian 09 program using the PBE1PBE keyword invoking the PBE0 functional and the 631G(d) basis set with the option opt=modredundant.

Dispersion-corrected DFT optimizations and electronic structure calculations on gas adsorption. Periodic DFT-D calculations were performed using CP2K[4] starting from the crystallographic coordinates of the saturated **NKU-FlexMOF-1a** systems for C_2H_6 and C_3H_8. In addition, an optimization was performed where the C_3H_8 molecules were first mutated to C_3H_6. These three calculations were performed using the MOLOPT basis sets for all atoms and the DFTD3 pair potential for dispersion

correction. The revPBE functional was used in periodic DFT with an applied pressure of 1.0 bar. The basis set was DZVP-MOLOPT-SR-GTH for Cu and DZVP-MOLOPT-GTH for all other atoms. The Cu atoms were treated in the singlet spin state (and thus so was the entire system). All atoms and the crystal cell parameters were allowed to relax using Conjugate Gradient minimization with CP2K's QUICKSTEP algorithm with no restraints applied using DIRECT_CELL_OPT (i.e. a full cell and geometry optimization).

The stress tensor at each step was computed analytically. The convergence criteria for each optimization step was 2.0×10^{-8} E_h during the SCF cycles. The overall optimization convergence criteria was 7.0×10^{-3} bohr for the maximum geometry change, 1.5×10^{-3} bohr for the root-mean-square geometry change, and 6.0×10^{-10} E_h per atom in the total energy change. An overlay of the optimized C_2H_6, C_3H_8, and C_3H_6 systems is shown in Figure S45. The binding energy per molecule was also calculated in the three optimized systems by the difference between the periodic DFT single point energies: $(E_{\text{NKU-FlexMOF-1a+gas}} - E_{\text{NKU-FlexMOF-1a}} - E_{\text{gas}})/4$, and the results are presented in Table S7. To further probe the properties of the experimental structures of the **NKU-FlexMOF-1a** systems, partial charges were calculated using a RESP fit of the electrostatic surface potential calculated on the final coordinates for the C_2H_6 and C_3H_8 crystallographic structures after emptying all sorbates and optimizing the position of the H atoms. The radii of the atoms were defined using the Universal Force Field[5] and the results are presented in Table S8.

Transient breakthrough of mixtures in fixed bed adsorbers. The performance of industrial fixed bed adsorbers is dictated by a combination of adsorption selectivity and uptake capacity. For a proper evaluation of **NKU-FlexMOF-1a**, we performed transient breakthrough simulations using the simulation methodology described in the literature.[6-9] For the breakthrough simulations, the following parameter values were used: length of packed bed, L = 0.3 m; voidage of packed bed, ε= 0.4; superficial gas velocity at inlet, u = 0.04 m/s. The transient breakthrough simulation results are presented in terms of a *dimensionless* time, τ, defined by dividing the actual time, t,

by the characteristic time, $\frac{L\varepsilon}{u}$.The feed mixture to the bed consists of a 50/50 (v/v) C_3H_6/C_3H_8 mixture at 258 K and 100 kPa. The concentrations of the two components exiting the bed, normalized with respect to the inlet feed concentrations are determined from the simulations.

Table S1. Crystal data and structure refinement parameters for **NKU-FlexMOF-1**.

	NKU-FlexMOF-1	
Formula	$C_{16}H_{13}CuFN_2O_5$	
*M*r (g mol^{-1})	395.83	
Space group	$P2_1/c$	
Crystal system	Monoclinic	
a (Å)	10.551(2)	
b (Å)	11.001(2)	
c (Å)	14.830(2)	
β(°)	108.79(3)	
V (Å^3)	1629.6(6)	
Z	4	
F(000)	804.0	
Dc (gcm^{-3})	1.613	
μ (mm^{-1})	1.381	
R_{int}	0.0917	
Limiting indices	$-13 \le h \le 13$ $-14 \le k \le 14$ $-19 \le l \le 19$	
GOF on F^2	1.131	
R_1, wR_2 [$I>2\sigma(I)$]^a	0.0741	0.1244
R_1, wR_2 [all data]^b	0.1177	0.1361

^{a} $R_1 = \sum ||F_o| - |F_c|| / \sum |F_o|$. ^{b} $wR_2 = \{\sum [w(F_o^2 - F_c^2)^2] / \sum w(F_o^2)^2\}^{1/2}$

Table S2. Crystal data and structure refinement parameters for **NKU-FlexMOF-1a**, **NKU-FlexMOF-1a-N_2-a**, **NKU-FlexMOF-1a-N_2-b**.

	NKU-FlexMOF-1a	**NKU-FlexMOF-1a-N_2-a**	**NKU-FlexMOF-1a-N_2-b**
Formula	$C_{13}H_6CuFNO_4$	$C_{52}H_{24}Cu_4F_4N_5O_{16}$	$C_{13}H_6CuFN_7O_4$
*M*r (g mol^{-1})	322.74	1304.96	406.80
Space group	$P2_1/c$	$P2_1/c$	$P2_1/c$
Crystal system	Monoclinic	Monoclinic	Monoclinic
a (Å)	10.4862(2)	10.488(2)	10.5629(2)
b (Å)	10.5374(3)	10.412(2)	11.3332(2)
c (Å)	15.0449(4)	15.057(6)	14.6254(3)
β(°)	106.838(3)	107.13(3)	108.254(2)
V ($Å^3$)	1591.15(8)	1571.3(6)	1662.72(6)
Z	4	1	4
F(000)	644	651	812
Dc (gcm^{-3})	1.347	1.379	1.625
μ (mm^{-1})	2.144	1.410	2.302
R_{int}	0.0324	0.0000	0.0281
Limiting indices	-12 ≤ h ≤ 9 -8≤ k ≤ 12 -17 ≤ l ≤17	0 ≤ h ≤ 14 0≤ k ≤ 14 -20 ≤ l ≤ 19	-11 ≤ h ≤ 012 -13≤ k ≤ 14 -18≤ l ≤ 16
GOF on F^2	1.044	1.109	1.041
R_1, wR_2 [$I>2\sigma(I)$][a]	0.0407 0.1014	0.0756 0.2463	0.0571 0.1605
R_1, wR_2 [all data][b]	0.0544 0.1070	0.0813 0.2517	0.0652 0.1666

[a] $R_1 = \sum ||F_o| - |F_c|| / \sum |F_o|$. [b] $wR_2 = \{\sum[w(F_o^2 - F_c^2)^2] / \sum w(F_o^2)^2\}^{1/2}$

Table S3. Crystal data and structure refinement parameters for **NKU-FlexMOF-1a-CO_2, NKU-FlexMOF-1a-C_2H_6, NKU-FlexMOF-1a-C_3H_8.**

	NKU-FlexMOF-1a-CO_2	**NKU-FlexMOF-1a-C_2H_6**	**NKU-FlexMOF-1a-C_3H_8**
Formula	$C_{15}H_6CuFNO_8$	$C_{53}H_{24}Cu_4F_4N_4O_{16}$	$C_{29}H_{22}Cu_2F_2N_2O_8$
*M*r (g mol^{-1})	410.76	1302.96	691.59
Space group	$P2_1/c$	$P2_1/c$	$P2_1/c$
Crystal system	Monoclinic	Monoclinic	Monoclinic
a (Å)	10.5570(8)	10.4890(3)	10.5743(7)
b (Å)	11.4035(9)	10.4486(4)	10.6558(7)
c (Å)	14.3239(12)	15.1078(7)	15.2273(12)
β(°)	108.725(9)	106.787(4)	108.493(8)
V (Å^3)	1633.1(2)	1585.18(11)	1627.2(2)
Z	4	1	2
F(000)	820	650	700
Dc (gcm^{-3})	1.671	1.365	1.411
μ (mm^{-1})	2.431	2.158	2.131
R_{int}	0.0607	0.1138	0.0795
Limiting indices	$-11 \le h \le 13$ $-14 \le k \le 13$ $-17 \le l \le 13$	$-13 \le h \le 12$ $-12 \le k \le 9$ $-16 \le l \le 18$	$-13 \le h \le 9$ $-12 \le k \le 13$ $-11 \le l \le 18$
GOF on F^2	1.061	1.190	1.095
R_1, wR_2 [$I>2\sigma(I)$][a]	0.0780 0.2068	0.1056 0.3028	0.1033 0.3179
R_1, wR_2 [all data][b]	0.0939 0.2265	0.1190 0.3176	0.1546 0.3438

[a] $R_1 = \sum ||F_o| - |F_c|| / \sum |F_o|$. [b] $wR_2 = \{\sum [w(F_o^2 - F_c^2)^2] / \sum w(F_o^2)^2\}^{1/2}$

Table S4. The content of Cu^{2+} in aqueous solutions with different pH measured by ICP.

H_2O	pH=3	pH=4	pH=10	pH=11
0.0061 ppm	0.0066 ppm	0.0068 ppm	0.0065 ppm	0.0064 ppm

Table S5. The unit cell parameters by the refinement of the *in situ* PXRD patterns of **NKU-FlexMOF-1a** at different N_2 pressure at 83 K.

P (kPa)	**a (Å)**	**b (Å)**	**c (Å)**	**β (°)**	**V (Å^3)**
1	10.526022	11.36439	14.540264	108.06349	1653.607
5	10.572457	11.377763	14.516596	108.37336	1657.197
10	10.589168	11.40171	14.533563	108.3859	1665.133
20	10.605217	11.426508	14.541866	108.27505	1673.311
40	10.607306	11.427928	14.543799	108.27545	1674.067
60	10.608903	11.430526	14.54851	108.26661	1675.328
80	10.62134	11.442893	14.555629	108.21493	1680.427
100	10.622354	11.446614	14.554541	108.21764	1680.983

Table S6. Breakthrough experiment at 1 bar at 273 K and 298 K.

	C_3H_6 Uptake(mmol/g)	C_3H_8 Uptake(mmol/g)	Selectivity (C_3H_6/ C_3H_8)
298 K	1.96	0.85	2.31
273 K	2.13	0.80	2.66

Table S7. Binding energy per molecule in periodic DFT optimized loaded systems after convergence.

System	Binding energy per molecule (kJ/mol)
NKU-FlexMOF-1a-C_2H_6	-41.
NKU-FlexMOF-1a-C_3H_8	-66.
NKU-FlexMOF-1a-C_3H_6	-59.

Table S8. Average partial charges by element calculated for framework atoms in H-optimized, emptied **NKU-FlexMOF-1a-C_2H_6** and **NKU-FlexMOF-1a-C_3H_8**. The partial charges are calculated in VASP on the experimentally determined crystal structures where the sorbates are removed in silico and only the hydrogen atom positions are optimized. It is clear that the electrostatic environment for the hydrocarbons is quite similar even for reasonably different molecules.

Element	**NKU-FlexMOF-1a-C_2H_6**	**NKU-FlexMOF-1a-C_3H_8**
Cu	0.8887	0.8666
C	0.0664	0.0649
N	-0.0918	-0.0494
O	-0.5920	-0.5903
F	-0.1714	-0.1729
H	0.1466	0.1454

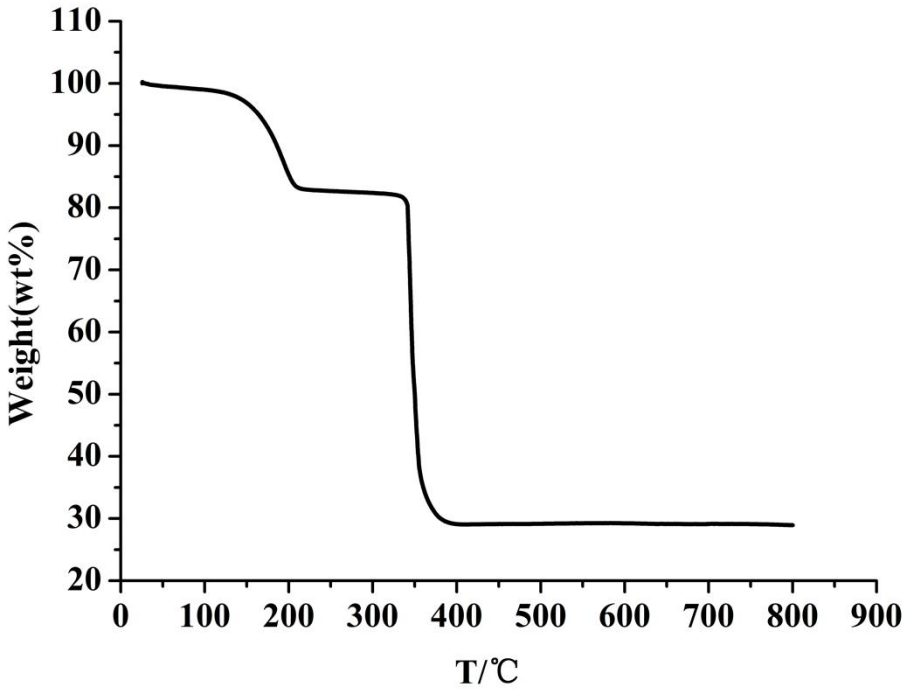

Figure S1. The TG curve of **NKU-FlexMOF-1**.

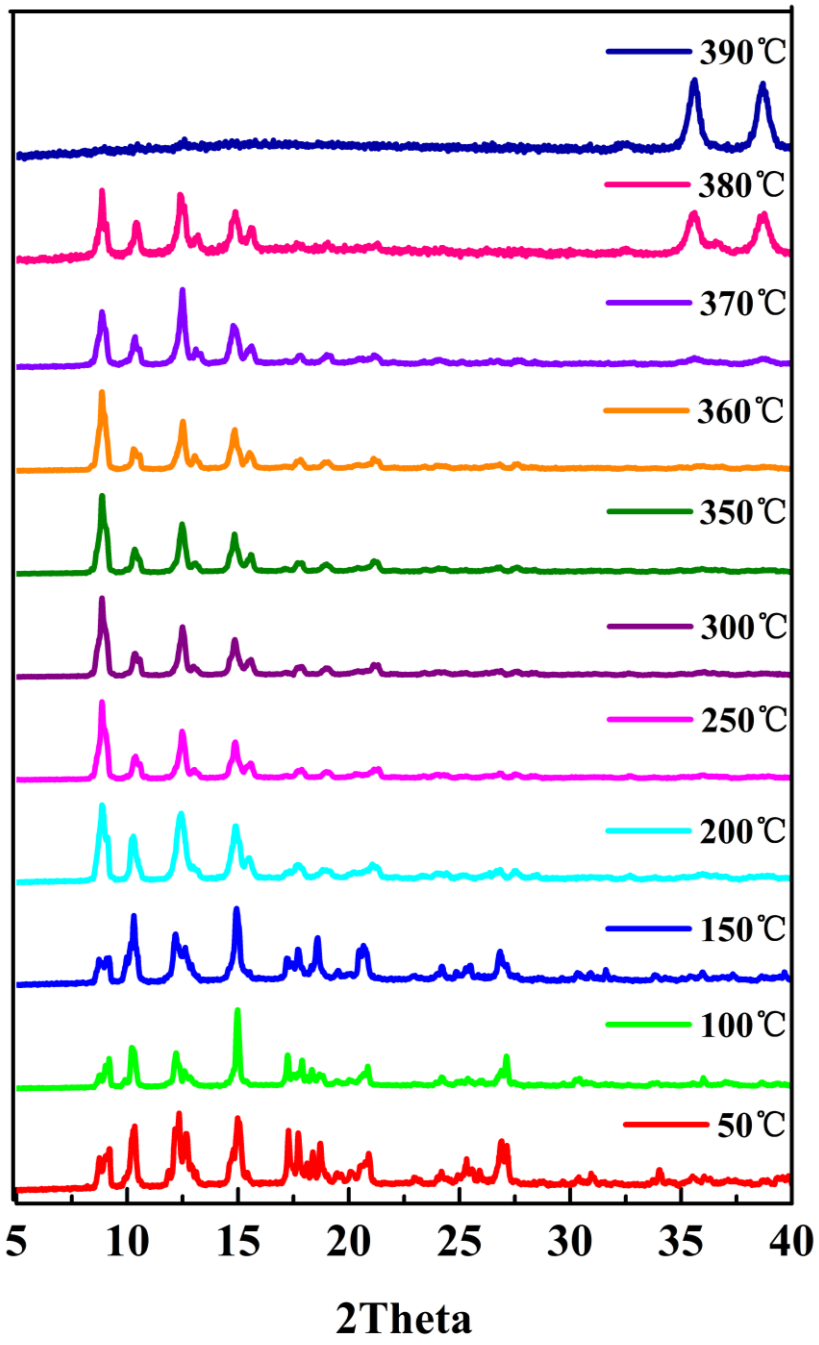

Figure S2. VT-PXRD patterns of **NKU-FlexMOF-1** under air atmosphere.

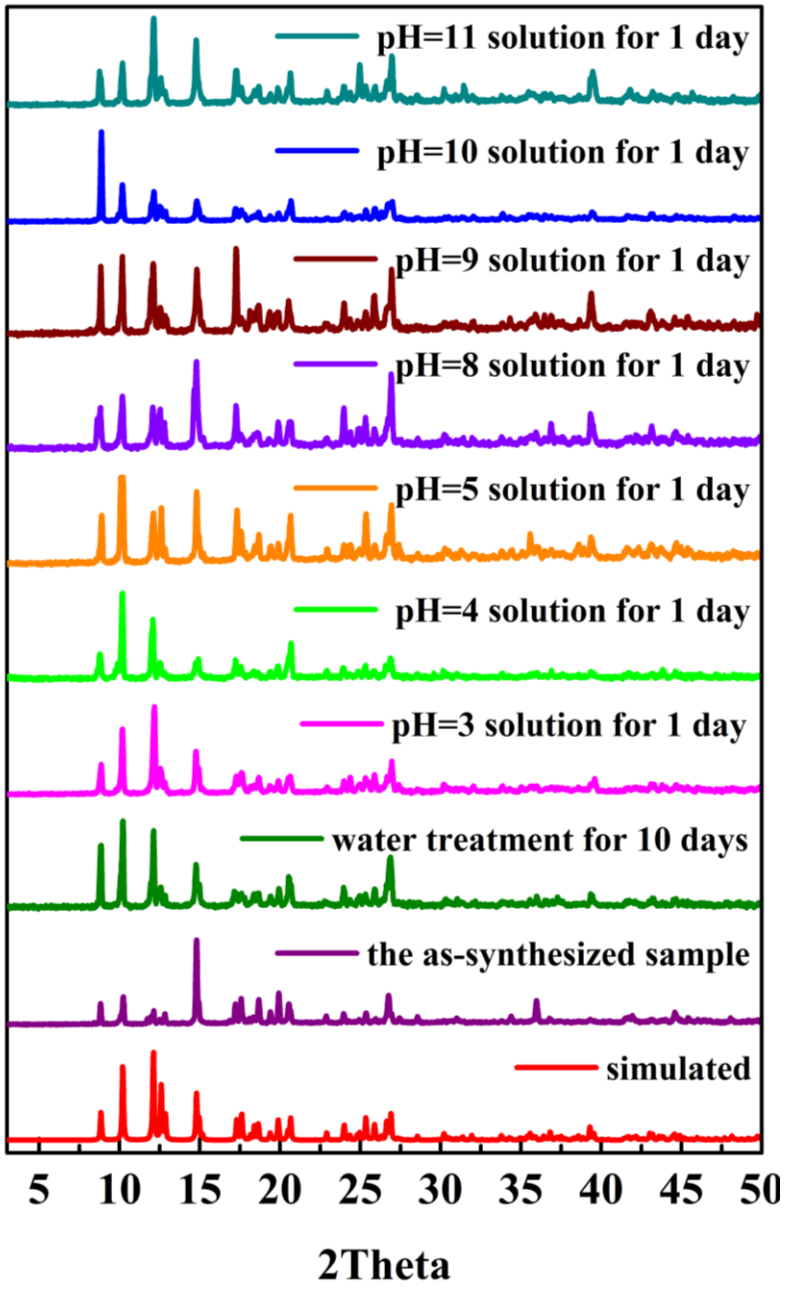

Figure S3. The PXRD patterns of the simulated patterns, the as-synthesized sample, after immersed in aqueous solution with different pH of **NKU-FlexMOF-1**.

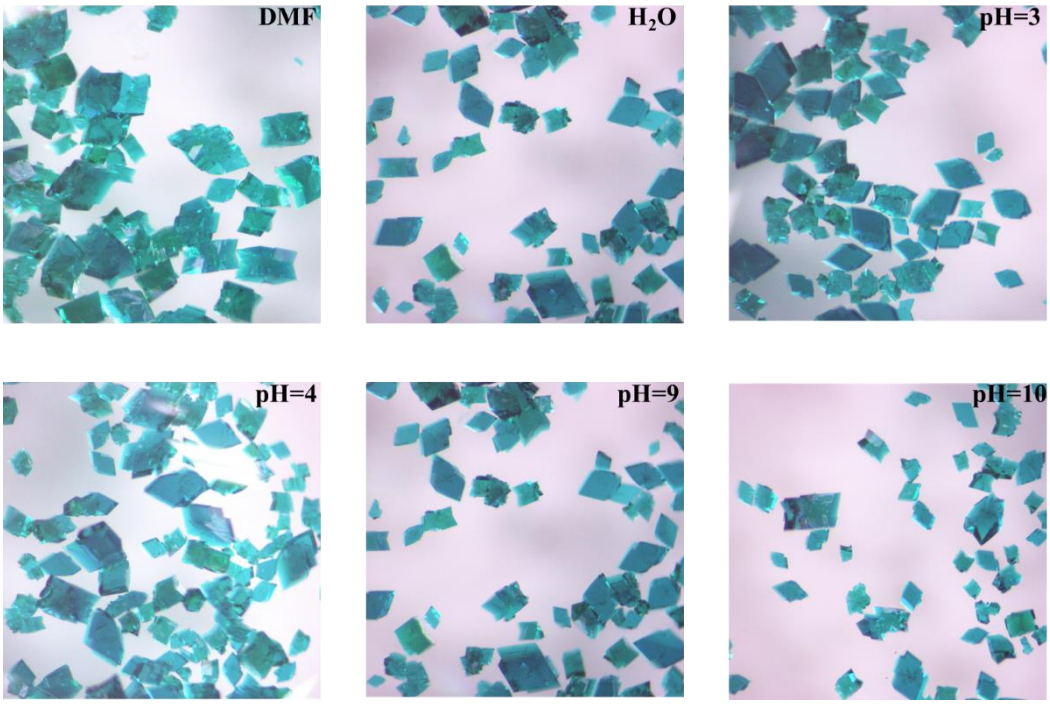

Figure S4. Optical microscope images of crystals of **NKU-FlexMOF-1** immersed in different pH aqueous solutions.

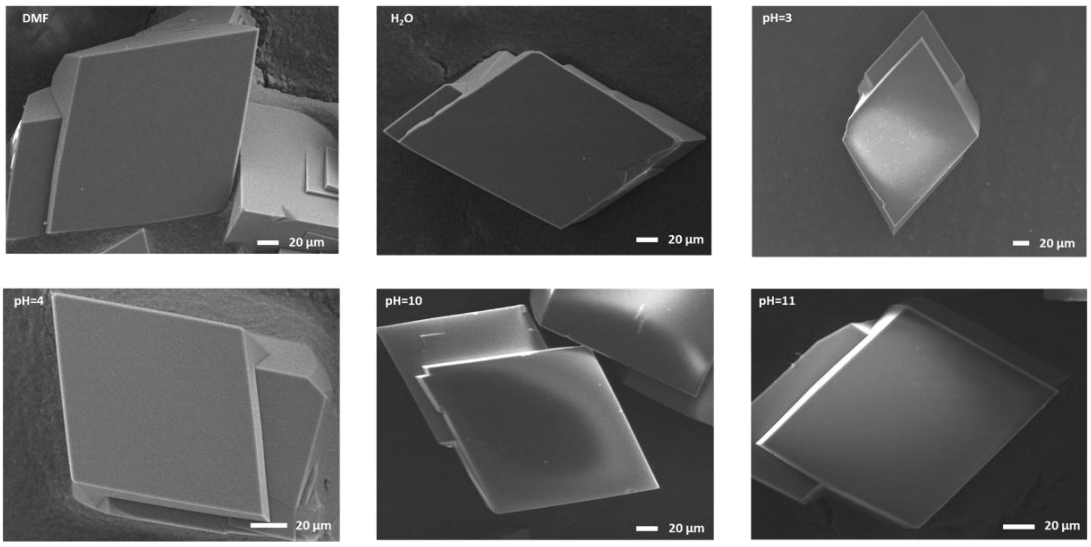

Figure S5. SEM images of crystals of **NKU-FlexMOF-1** immersed in different pH aqueous solutions.

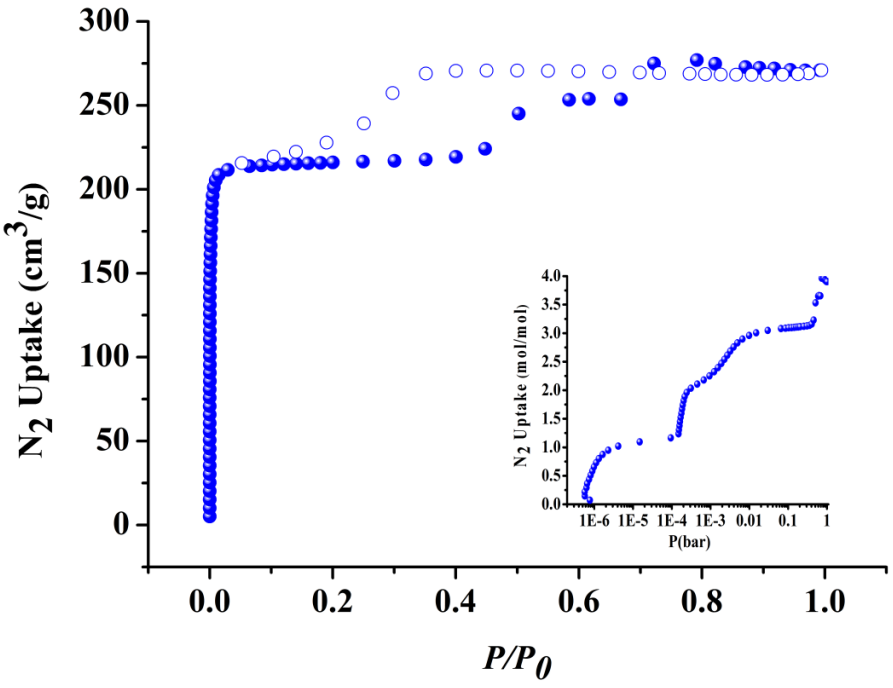

Figure S6. Volumetric N_2 adsorption isotherm of **NKU-FlexMOF-1a** at 77 K.

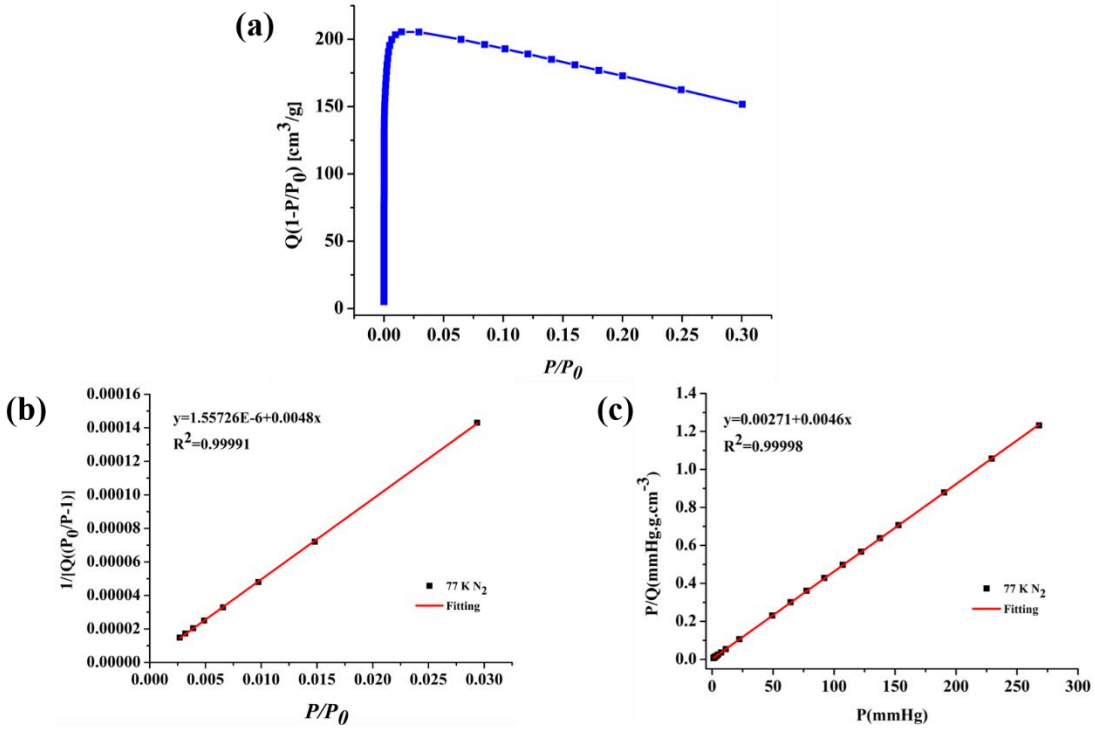

S_{BET} = [1/(0.0048-0.00000155726)]/22414 ×6.023 ×10^{23} ×0.170 ×10^{-18} = 952 m^2g^{-1}.

$S_{Langmuir}$ = [(1/0.0046) /22414] ×6.023 ×10^{23} ×0.170 ×10^{-18} = 993 m^2g^{-1}.

Figure S7. (a) Plot of the term $Q(1-P/P_0)$ vs P/P_0. (b) The BET and (c) Langmuir surface areas of **NKU-FlexMOF-1a** obtained from the N_2 adsorption isotherm at 77 K.

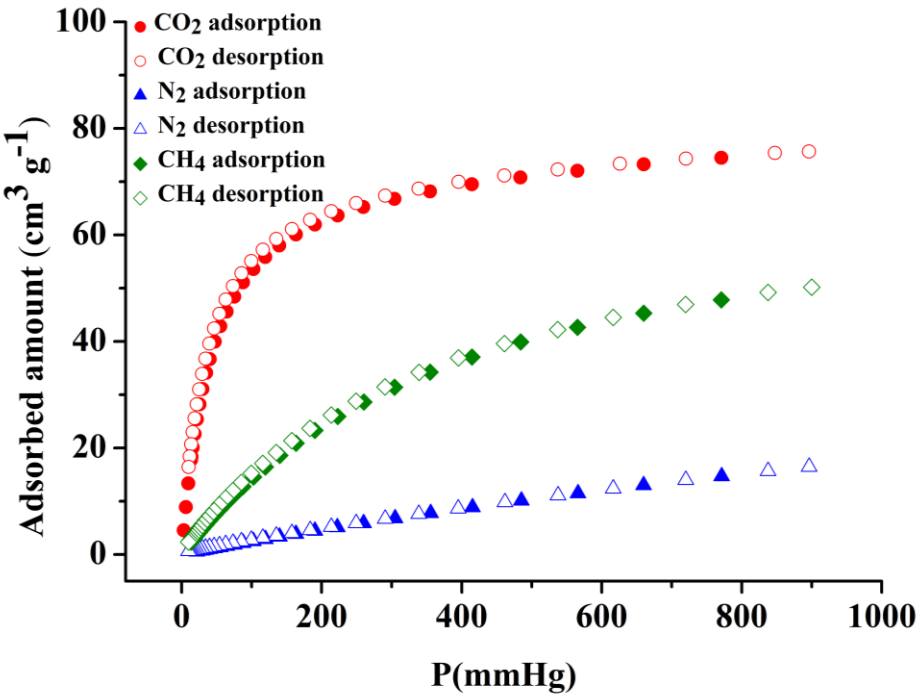

Figure S8. CO_2, CH_4 and N_2 adsorption isotherms of **NKU-FlexMOF-1a** at 273 K.

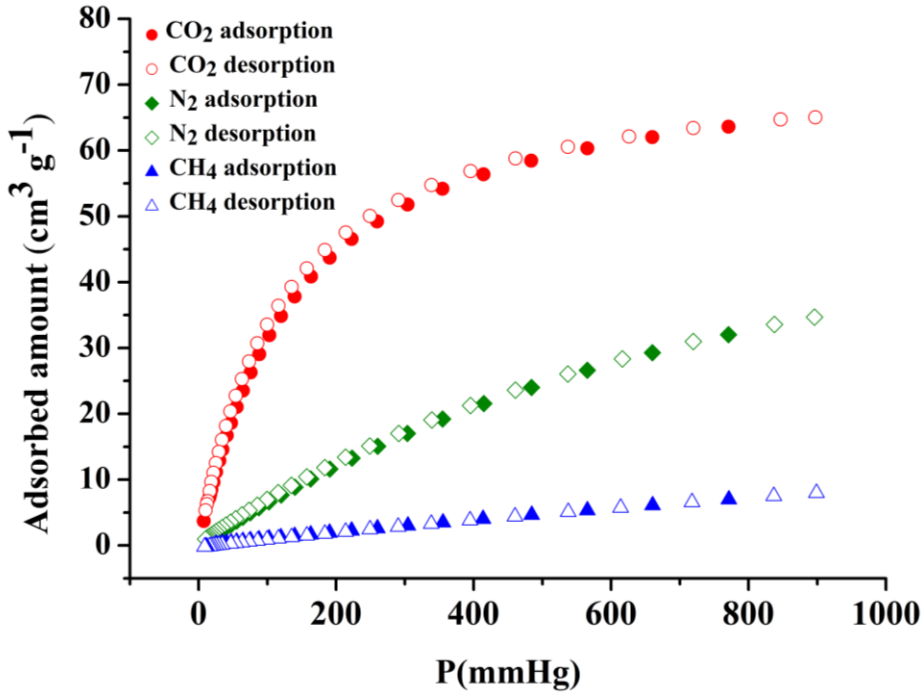

Figure S9. CO_2, CH_4 and N_2 adsorption isotherms of **NKU-FlexMOF-1a** at 298 K.

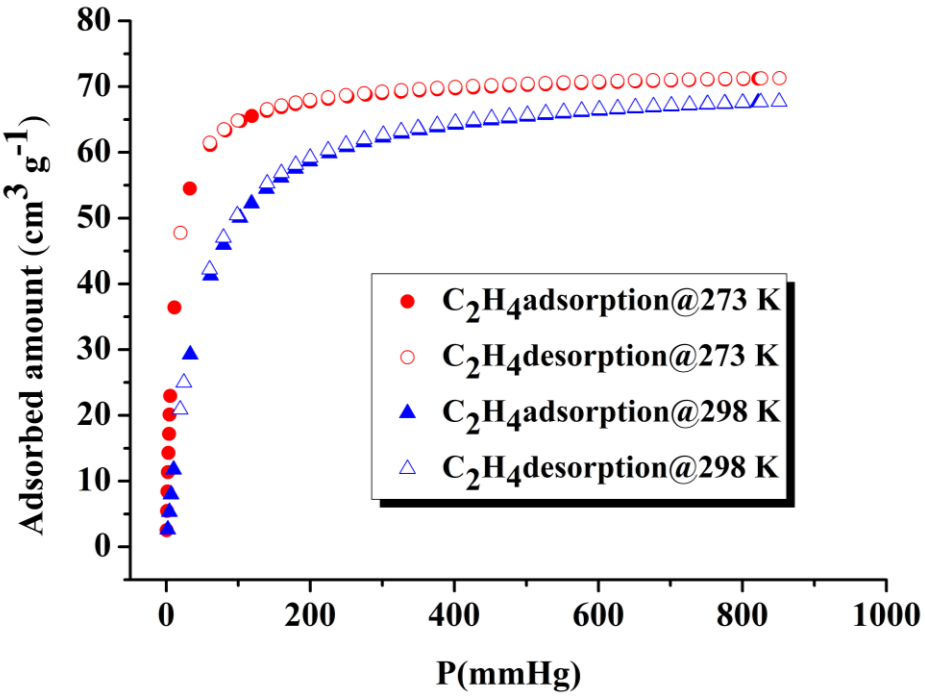

Figure S10. C_2H_4 adsorption isotherms of **NKU-FlexMOF-1a** at 273 K and 298 K.

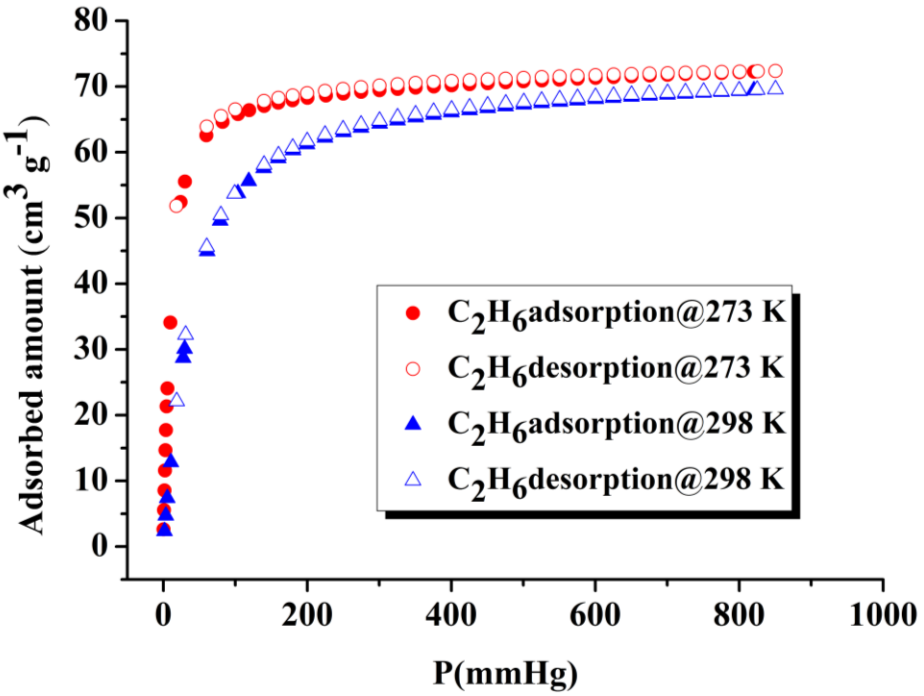

Figure S11. C_2H_6 adsorption isotherms of **NKU-FlexMOF-1a** at 273 K and 298 K.

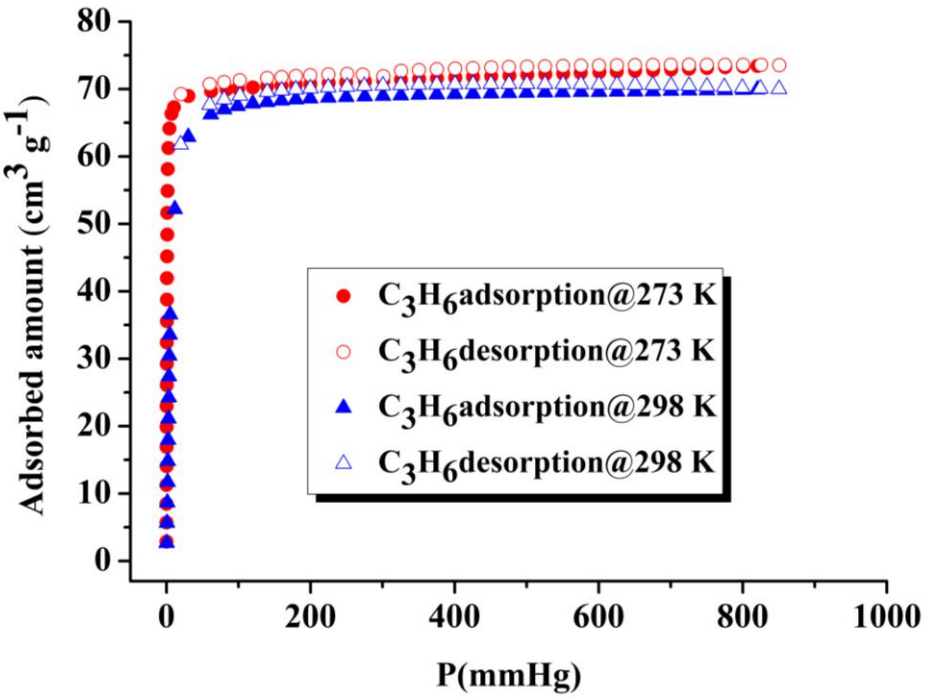

Figure S12. C_3H_6 adsorption isotherms of **NKU-FlexMOF-1a** at 273 K and 298 K.

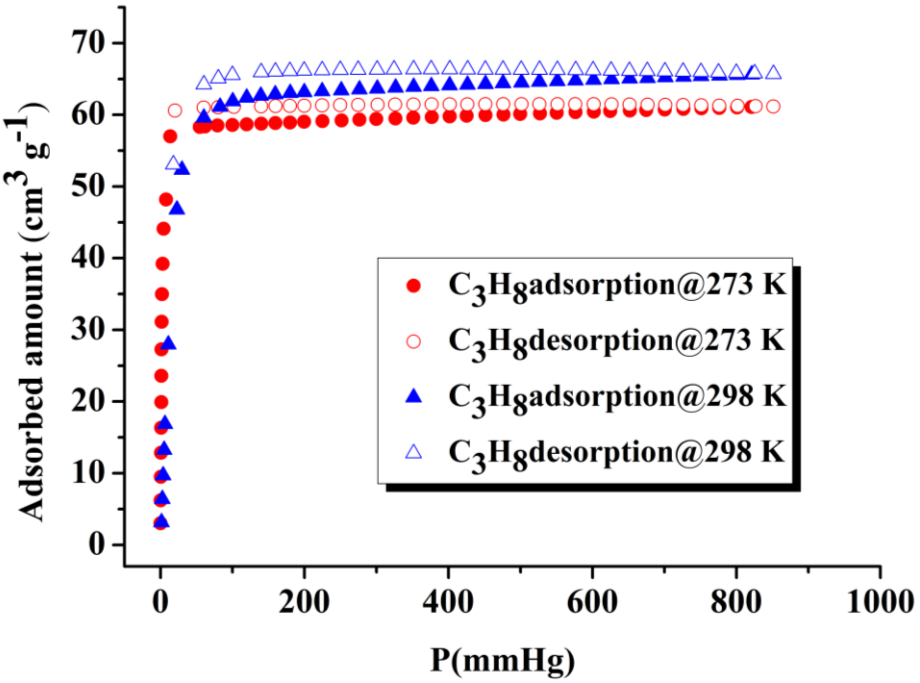

Figure S13. C_3H_8 adsorption isotherms of **NKU-FlexMOF-1a** at 273 K and 298 K.

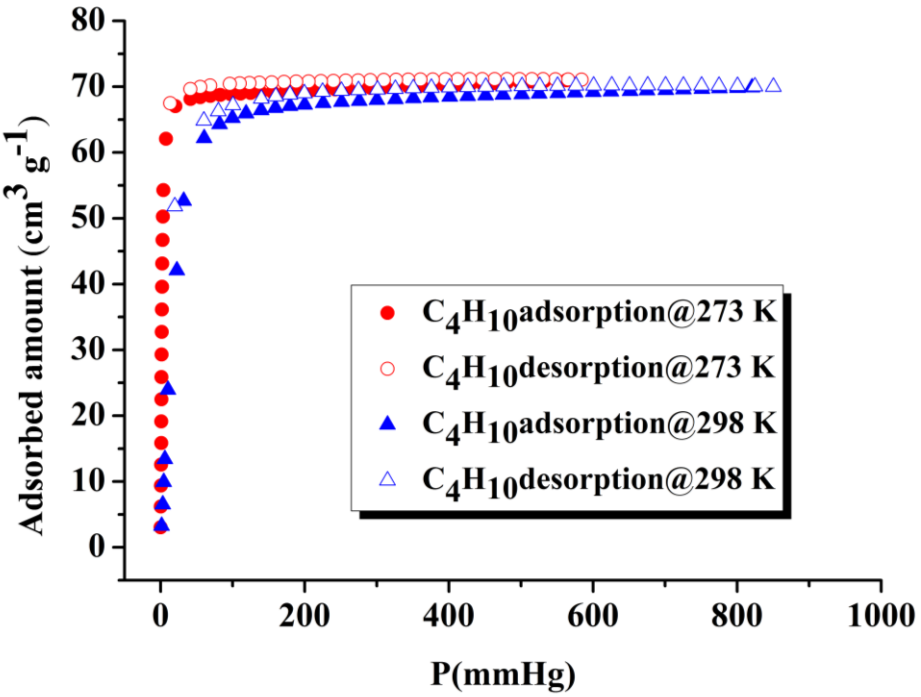

Figure S14. C_4H_{10} adsorption isotherms of **NKU-FlexMOF-1a** at 273 K and 298 K.

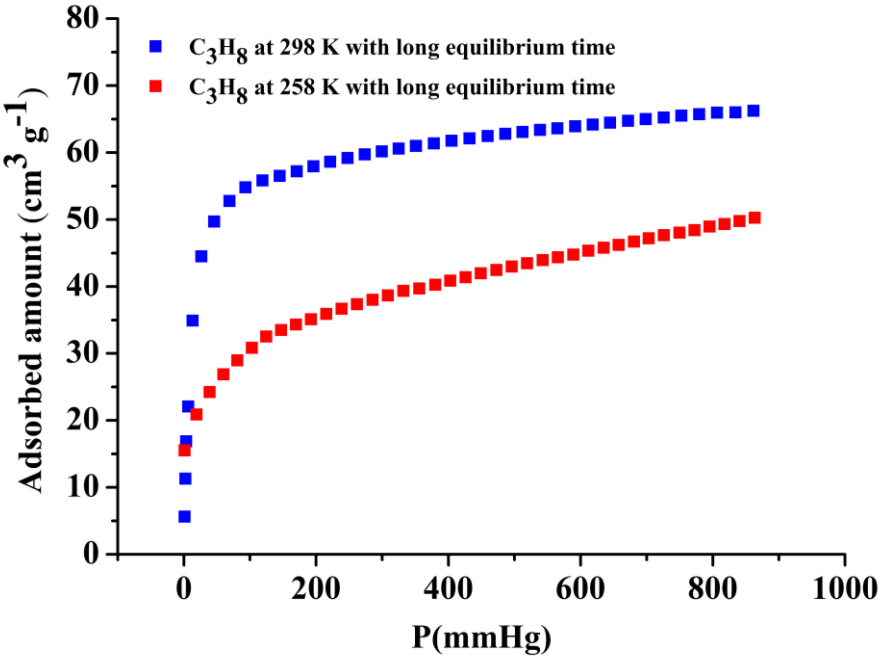

Figure S15. C_3H_8 adsorption isotherms of **NKU-FlexMOF-1a** at 258 and 298 K with long equilibrium time (intervals between two points at least 124 minutes).

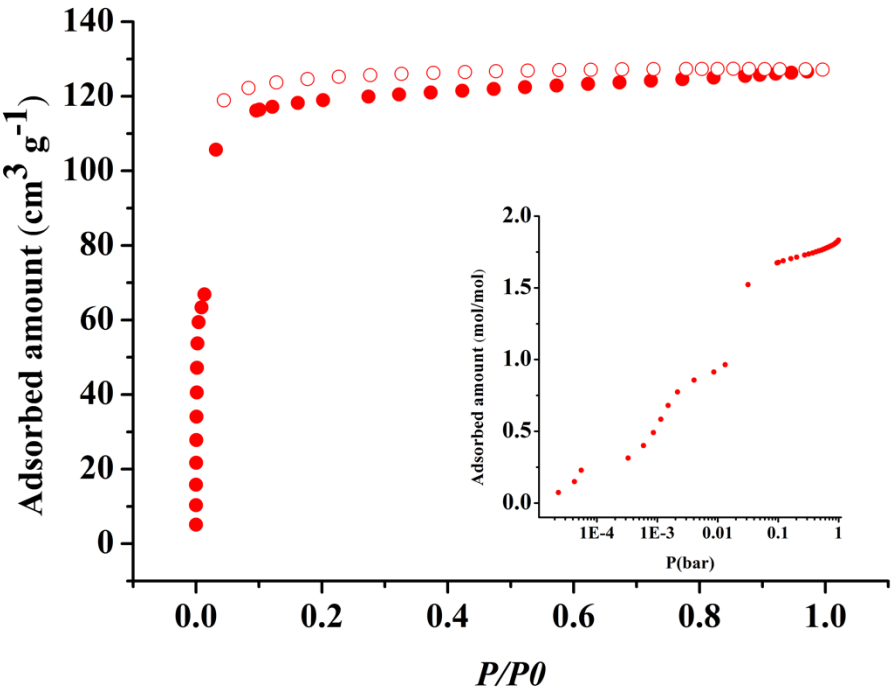

Figure S16. Volumetric CO_2 adsorption isotherm of **NKU-FlexMOF-1a** at 195 K after activation from **NKU-FlexMOF-1**.

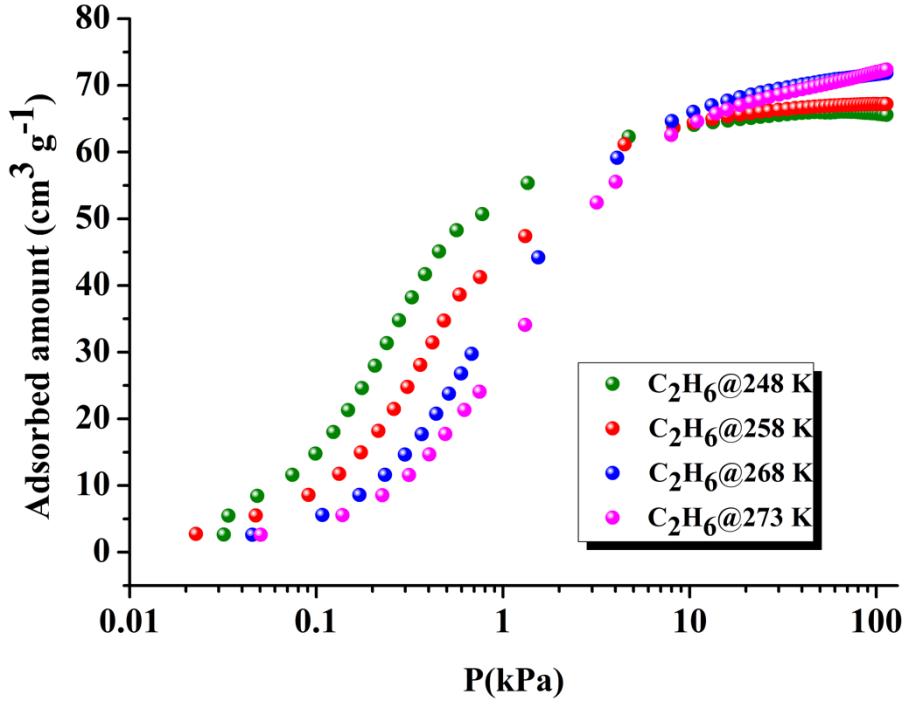

Figure S17. Low-pressure adsorption points for C_2H_6 at 248-273 K.

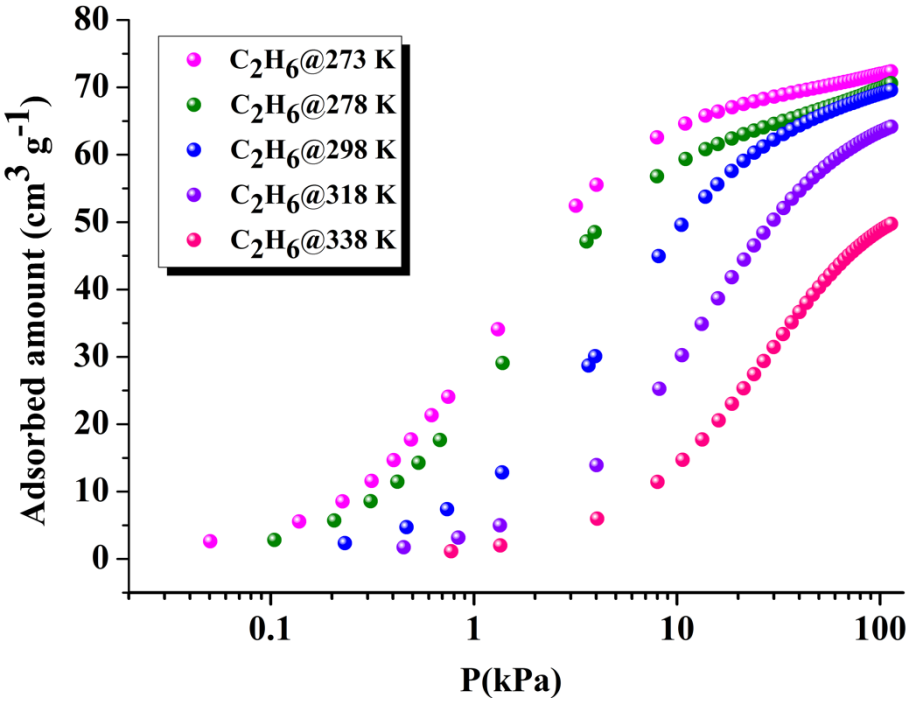

Figure S18. Low-pressure adsorption points for C_2H_6 at 273-338 K.

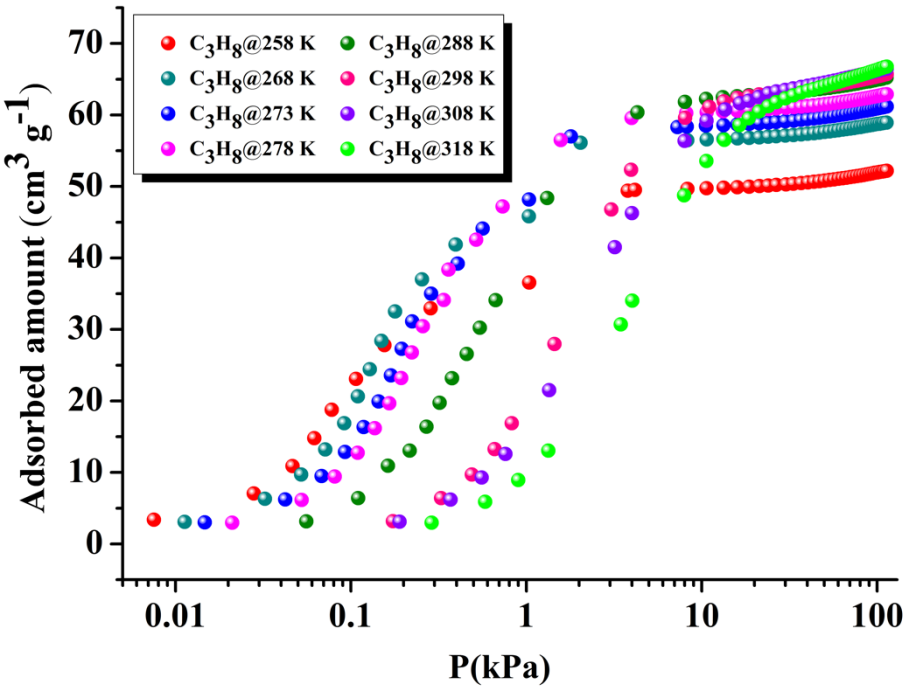

Figure S19. Low-pressure adsorption points for C_3H_8 at 258-318 K.

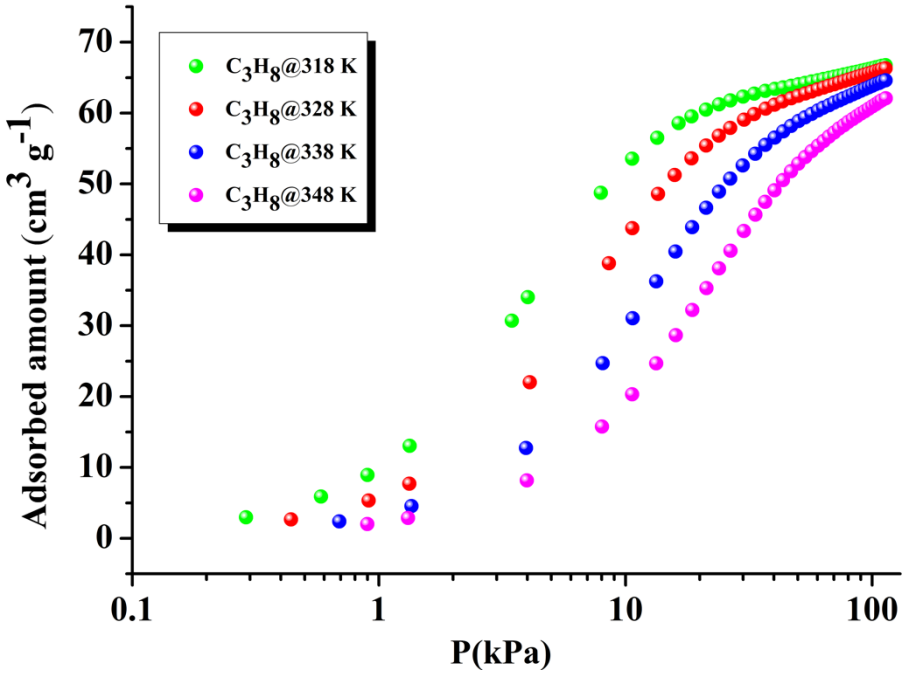

Figure S20. Low-pressure adsorption points for C_3H_8 at 318-348 K.

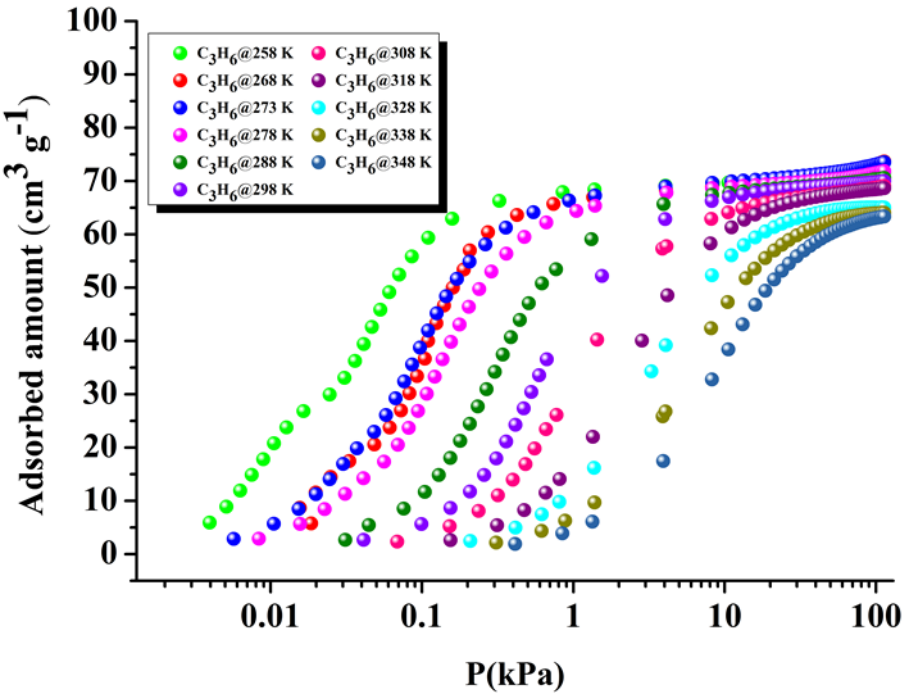

Figure S21. Low-pressure adsorption points for C_3H_6 at 258-348 K.

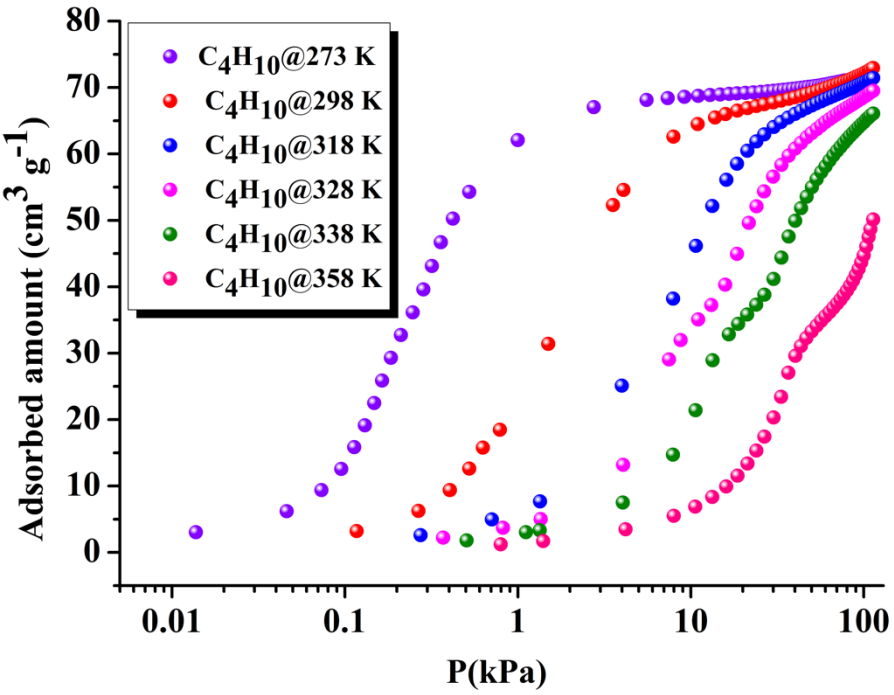

Figure S22. Low-pressure adsorption points for C_4H_{10} at 273-358 K.

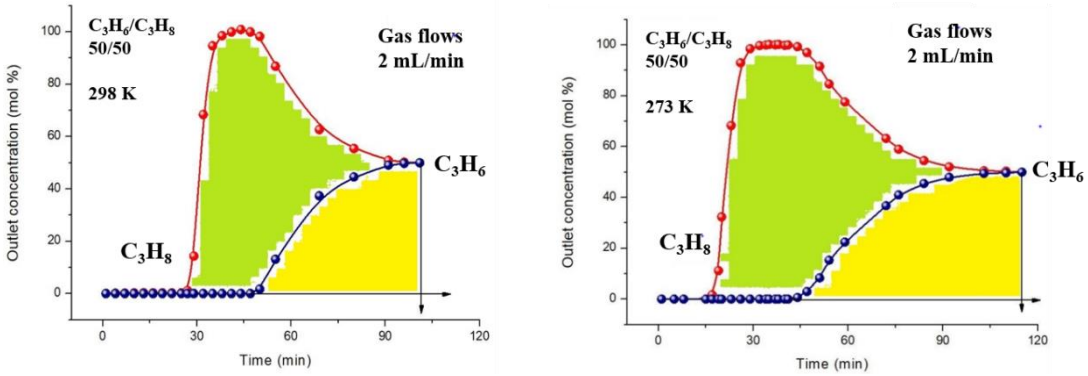

Figure S23. Calculated C_3H_6/C_3H_8 selectivity in dynamic condition is 2.31 at 298 K and is 2.66 at 273 K.

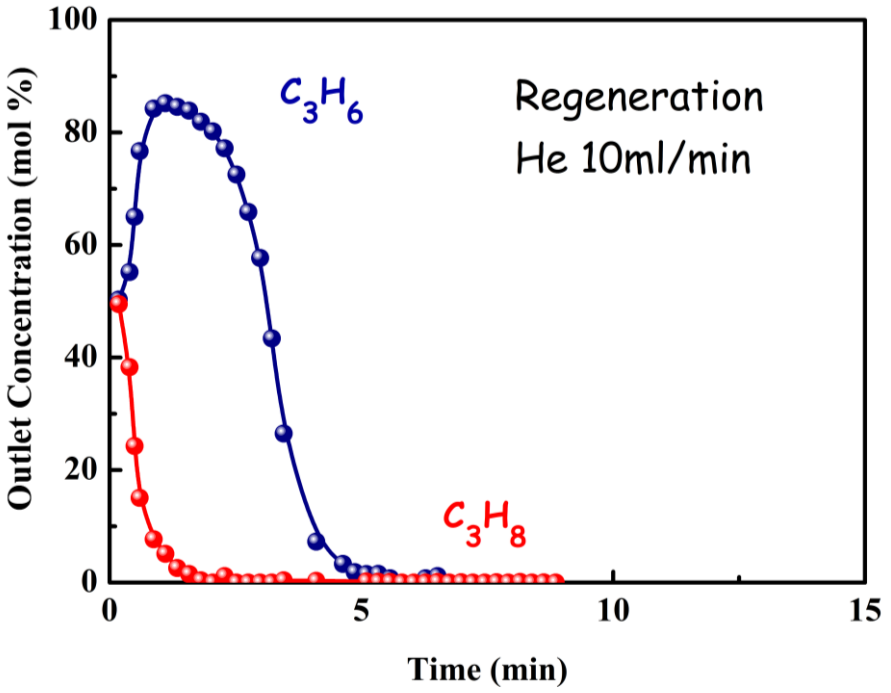

Figure S24. The components of desorbed C_3H_6/C_3H_8 mixture following the breakthrough experiment.

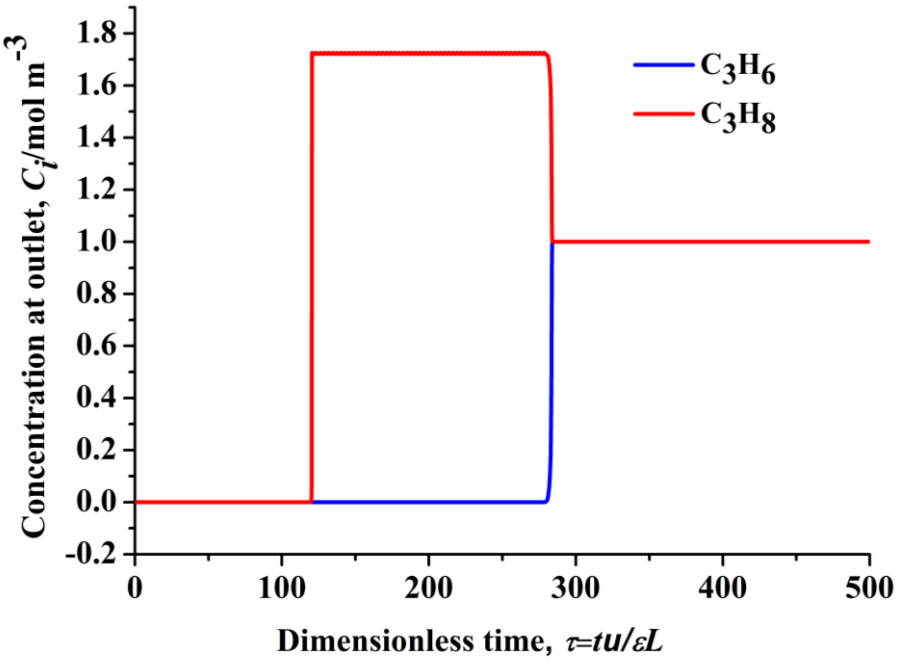

Figure S25. Transient breakthrough curve of the bed consists of a 50/50 C_3H_6/C_3H_8 mixture in an adsorbed bed packed with **NKU-FlexMOF-1a** at 258 K. For the breakthrough simulations, the following parameters were used, L = 0.3 m; ε = 0.4; u = 0.04 m s^{-1}.

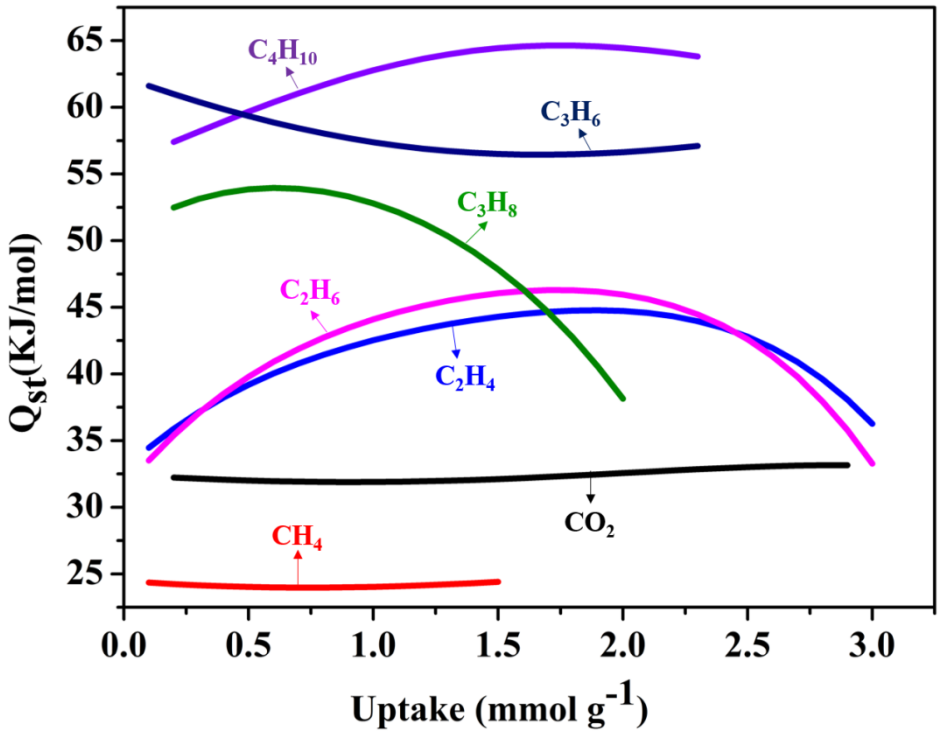

Figure S26a. Isosteric heats (Q_{st}) of CO_2, CH_4, C_2H_4, C_2H_6, C_3H_8 and C_4H_{10} adsorption for **NKU-FlexMOF-1a** estimated from virial expression fits at 273 and 298 K.

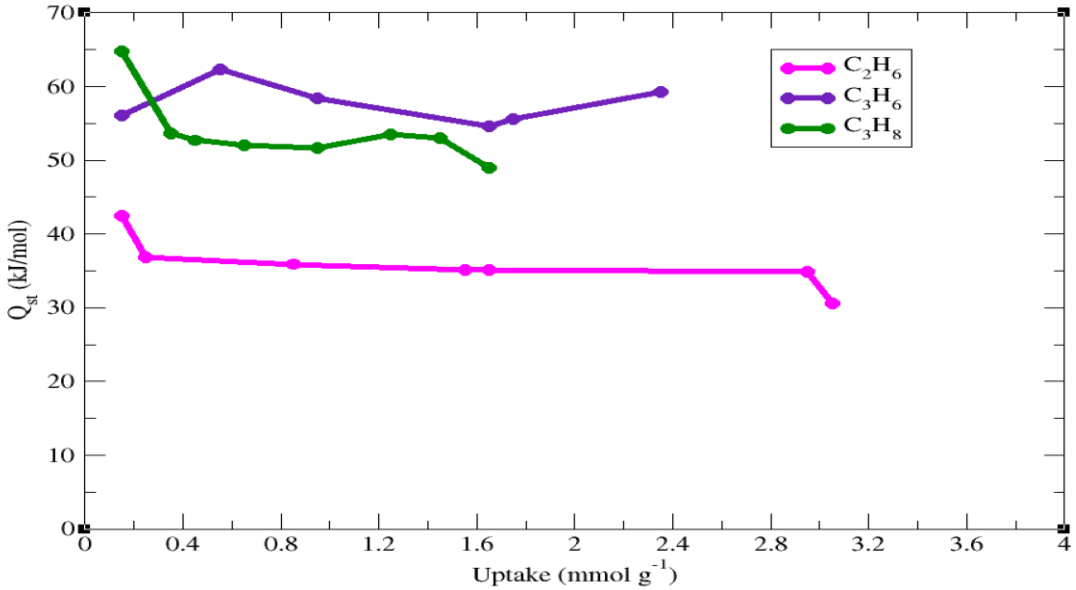

Figure S26b. Isosteric heats (Q_{st}) of C_2H_6, C_3H_8 and C_3H_6 adsorption for **NKU-FlexMOF-1a** estimated from the integrated Clausis-Clayperon expression, *lnP=-Qst/(RT)+C*. This method is formally equivalent but preferable in practice for a material where the framework is changing continuously in reaction to the framework. Linear fits are used plotting lnP vs 1/T to extract Q_{st} via the slope. Here the same temperatures, 273 K, 298 K, as in pane (a). The full data set was plotted and seen to be linear of the full temperature range of interest.

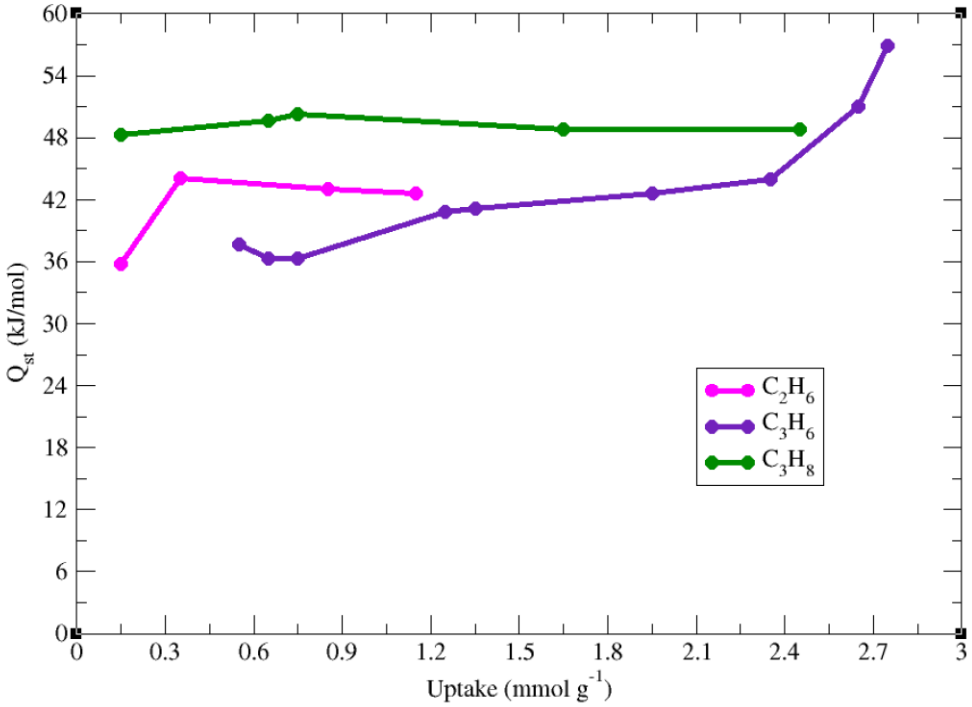

Figure S26c. Same as (b) using 328 and 348 K.

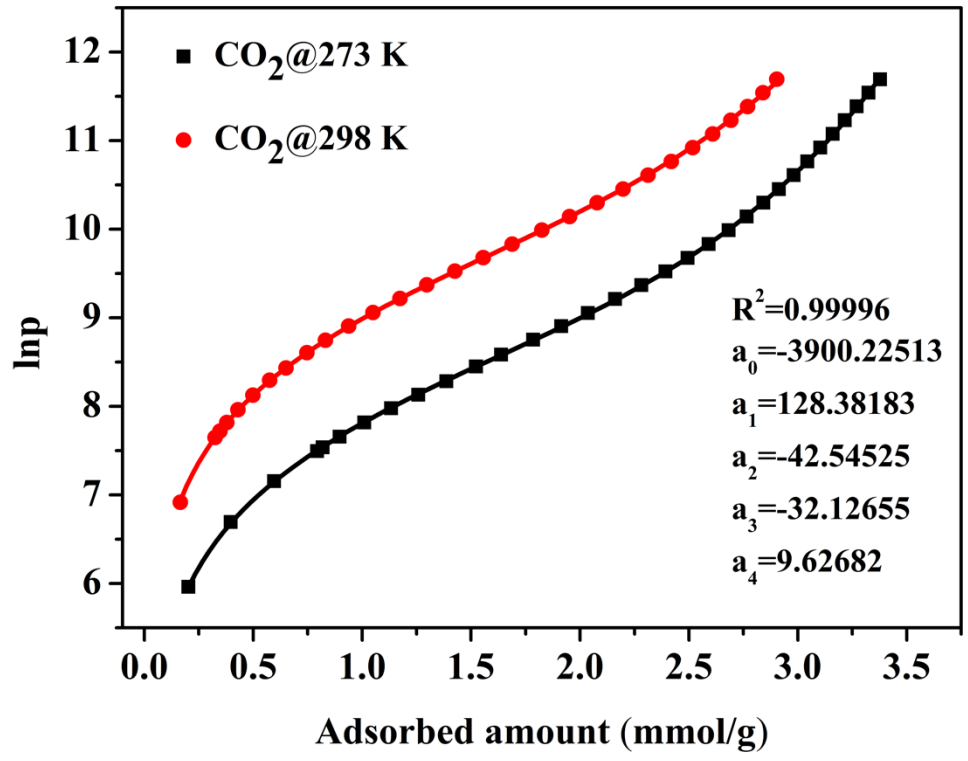

Figure S27. The details of virial equation (solid lines) fitting to the experimental CO_2 adsorption data (symbols) for **NKU-FlexMOF-1a**.

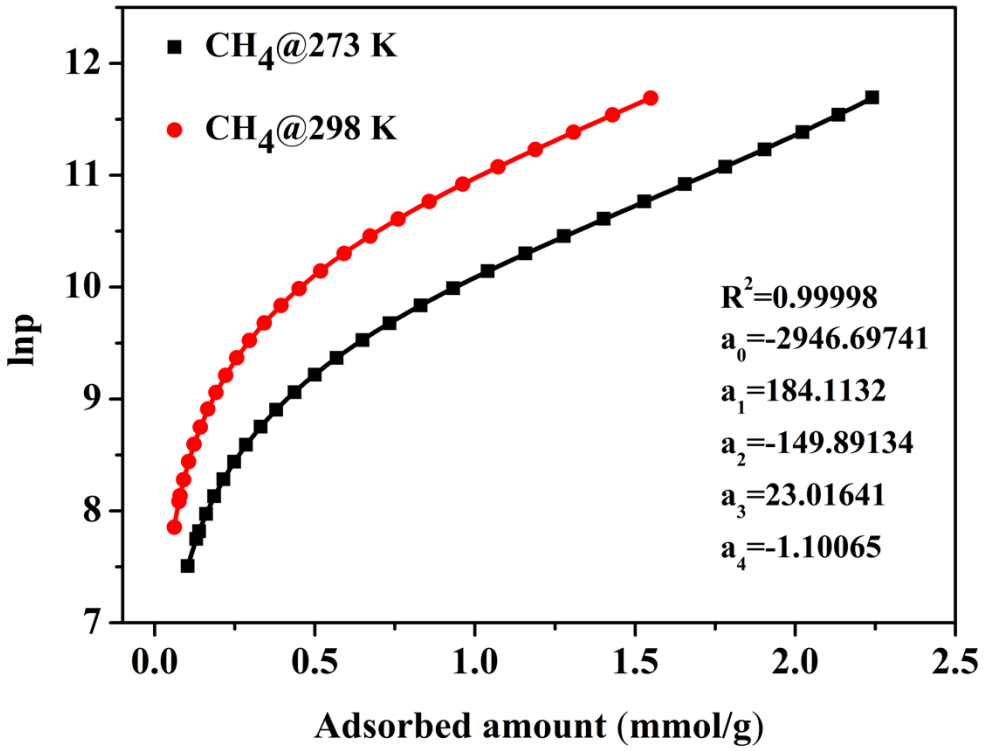

Figure S28. The details of virial equation (solid lines) fitting to the experimental CH_4 adsorption data (symbols) for **NKU-FlexMOF-1a**.

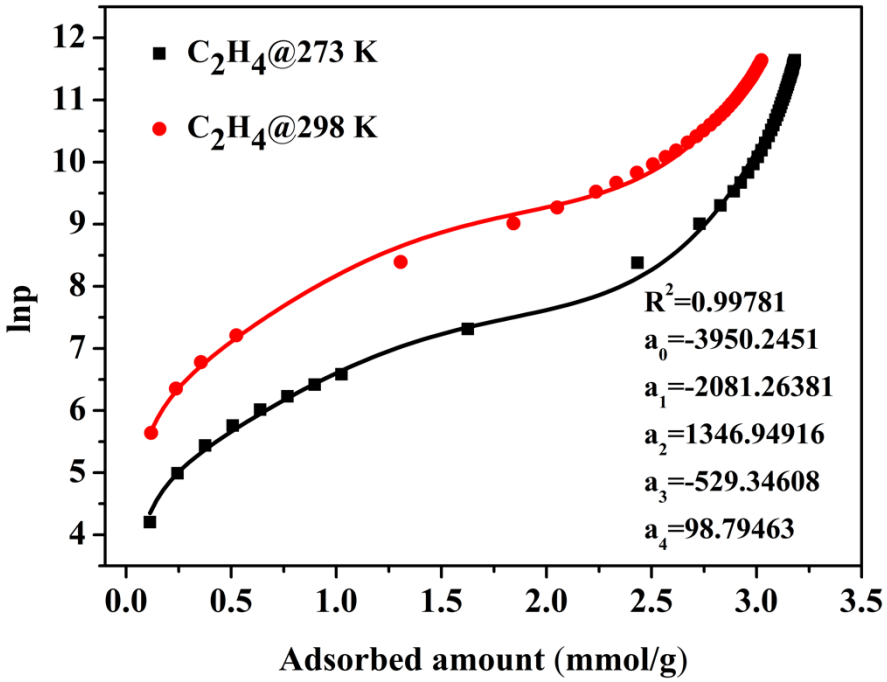

Figure S29. The details of virial equation (solid lines) fitting to the experimental C_2H_4 adsorption data (symbols) for **NKU-FlexMOF-1a**.

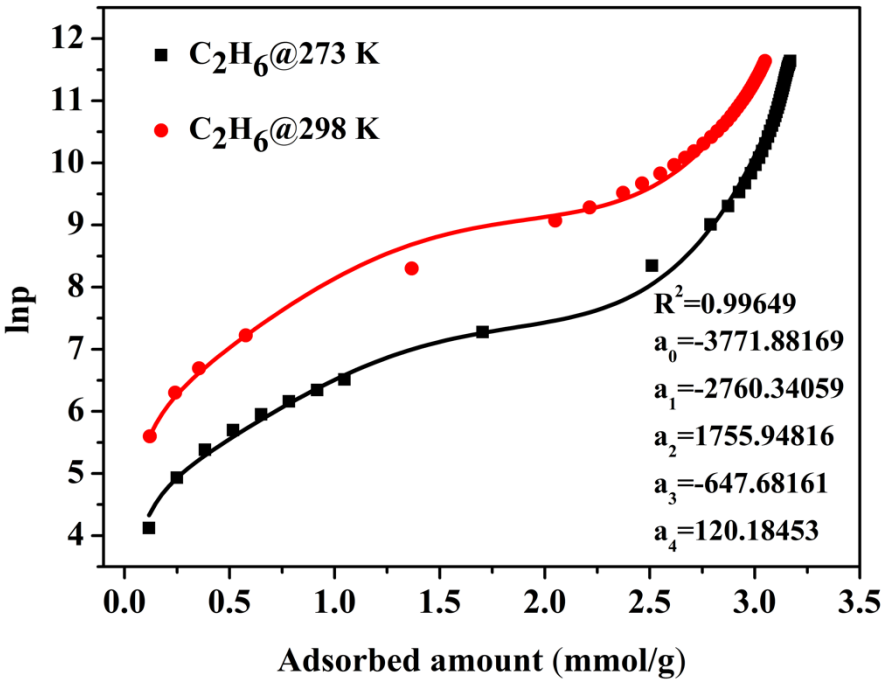

Figure S30. The details of virial equation (solid lines) fitting to the experimental C_2H_6 adsorption data (symbols) for **NKU-FlexMOF-1a**.

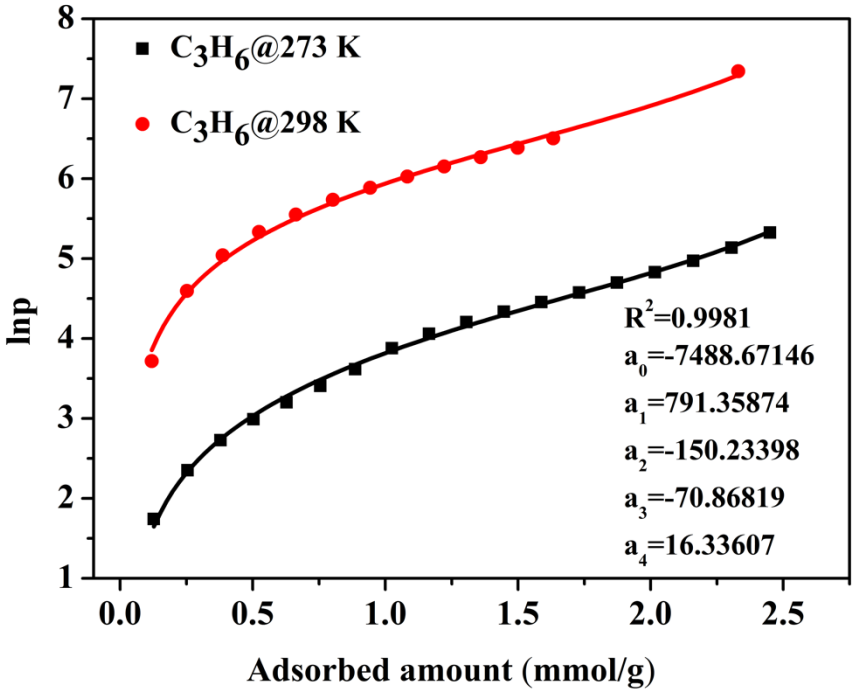

Figure S31. The details of virial equation (solid lines) fitting to the experimental C_3H_6 adsorption data (symbols) for **NKU-FlexMOF-1a**.

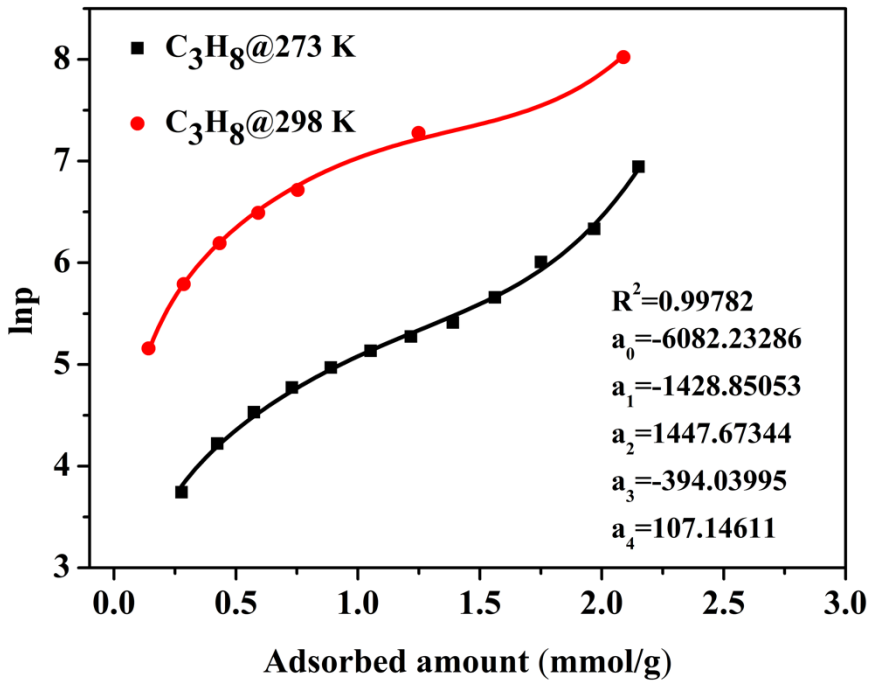

Figure S32. The details of virial equation (solid lines) fitting to the experimental C_3H_8 adsorption data (symbols) for **NKU-FlexMOF-1a**.

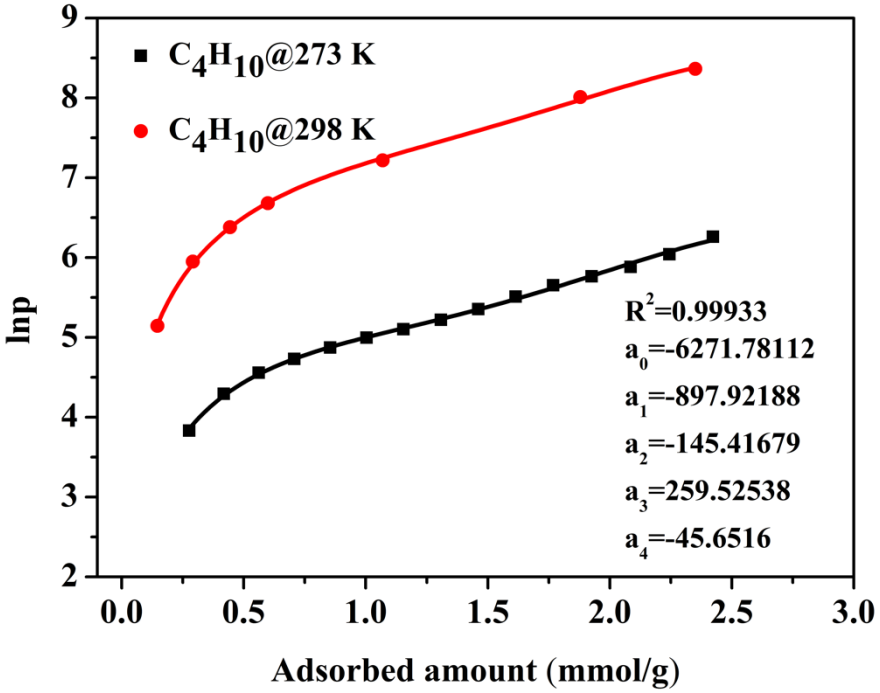

Figure S33. The details of virial equation (solid lines) fitting to the experimental C_4H_{10} adsorption data (symbols) for **NKU-FlexMOF-1a**.

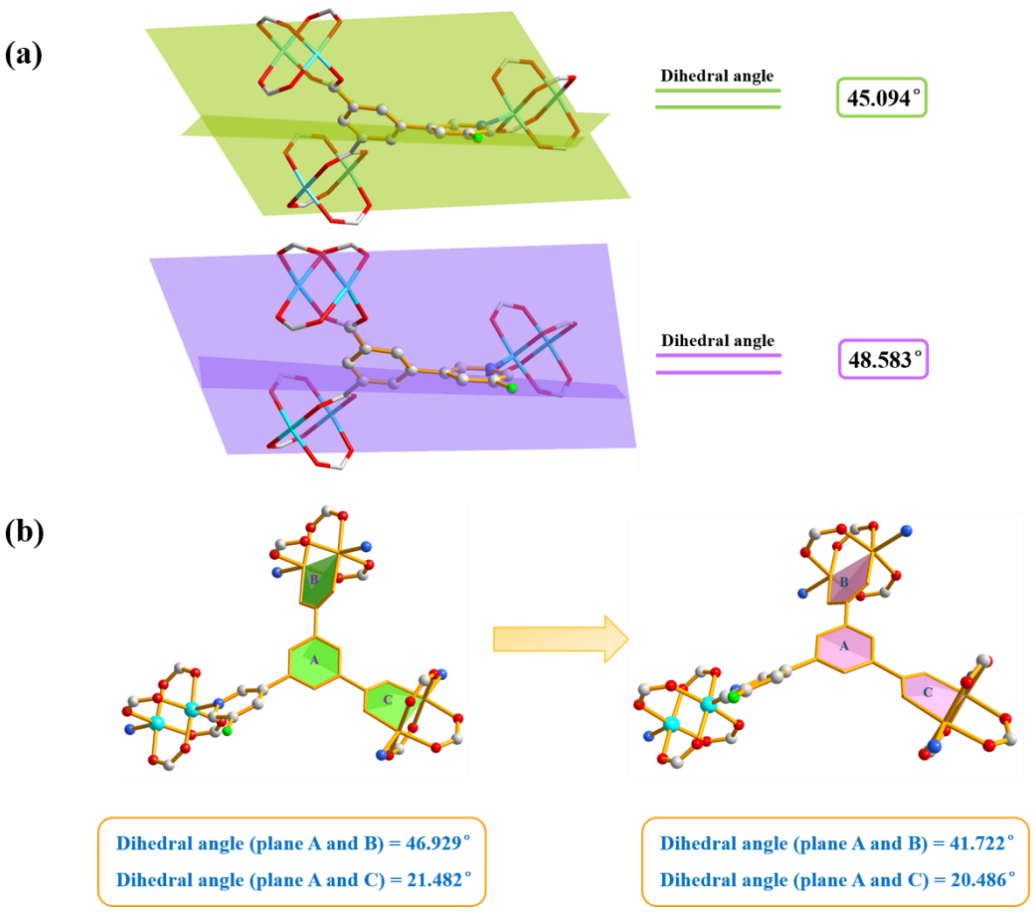

Figure S34. The structure analysis. (a) The dihedral angle between pyridyl and phenyl rings for **NKU-FlexMOF-1a-N_2-a** and **NKU-FlexMOF-1a-N_2-b**. (b) The dihedral angles between phenyl rings and paddle-wheel SBU for **NKU-FlexMOF-1a-N_2-a** and **NKU-FlexMOF-1a-N_2-b**.

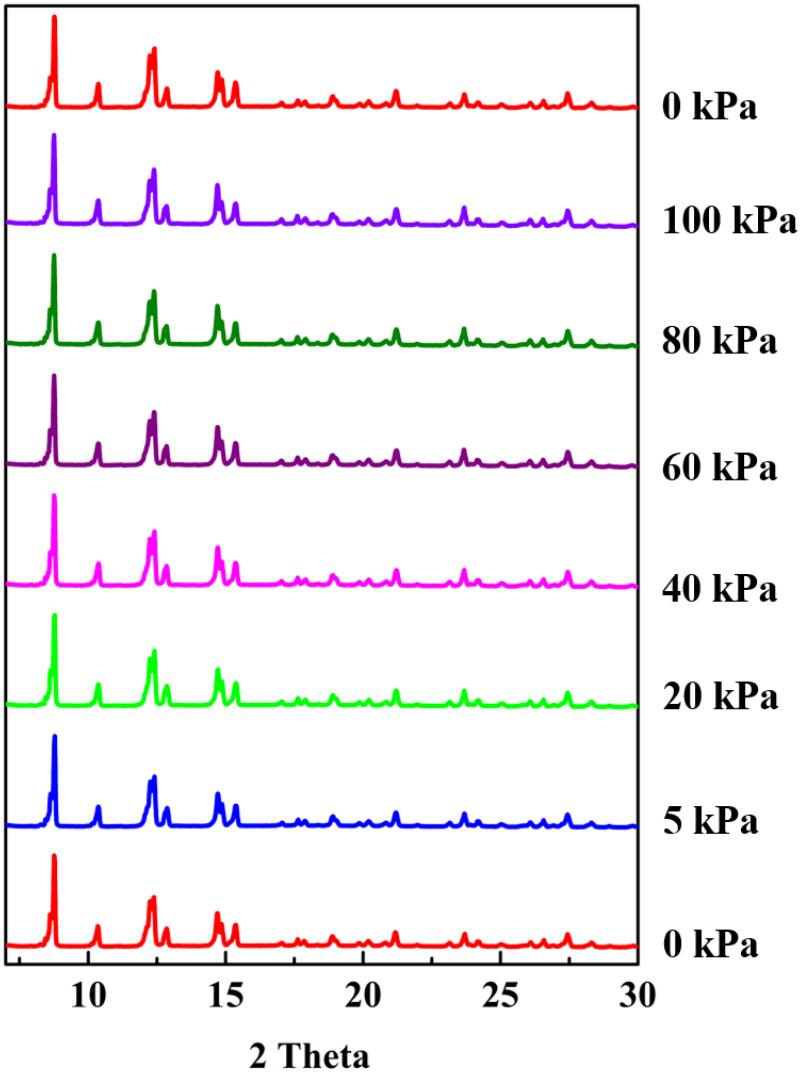

Figure S35. *In situ* powder X-ray diffraction patterns are shown for **NKU-FlexMOF-1a** at 273 K and variable N_2 pressures.

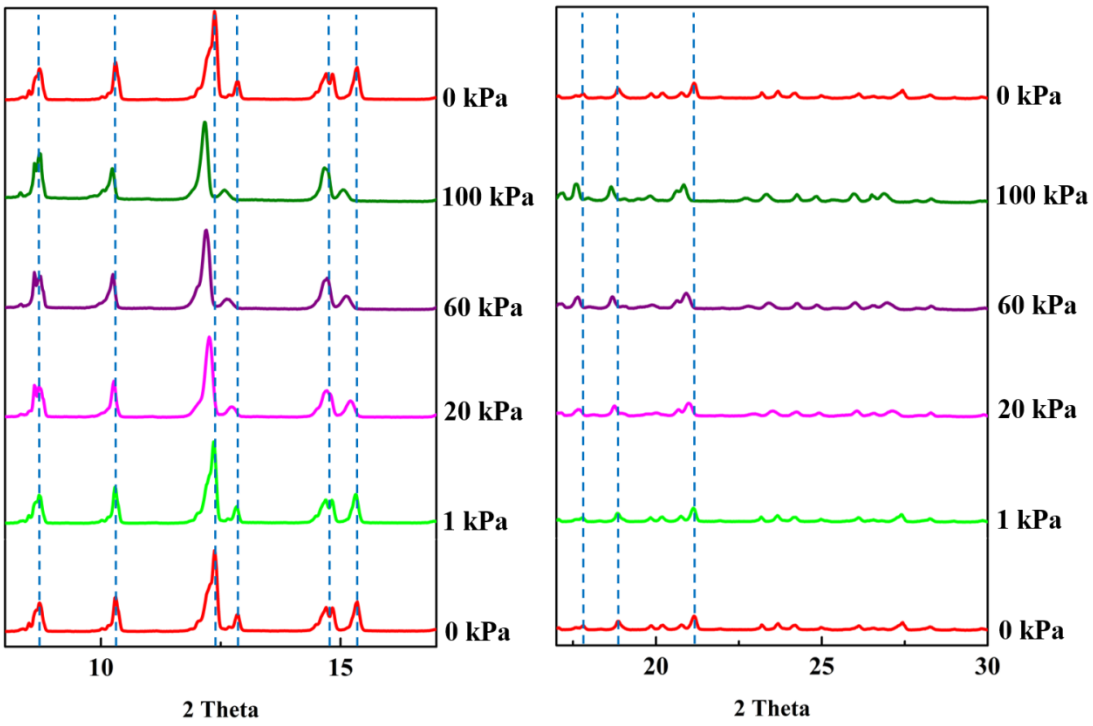

Figure S36. *In situ* powder X-ray diffraction patterns are shown for **NKU-FlexMOF-1a** at room temperature and variable C_3H_8 pressures.

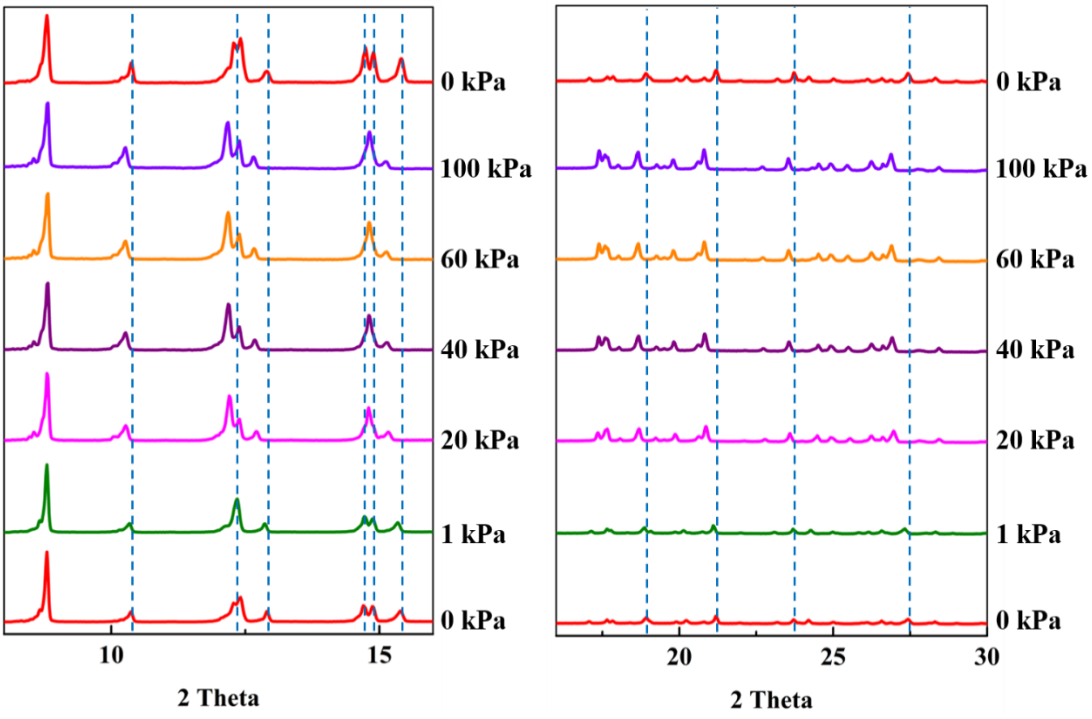

Figure S37. *In situ* powder X-ray diffraction patterns are shown for **NKU-FlexMOF-1a** at room temperature and variable C_3H_6 pressures.

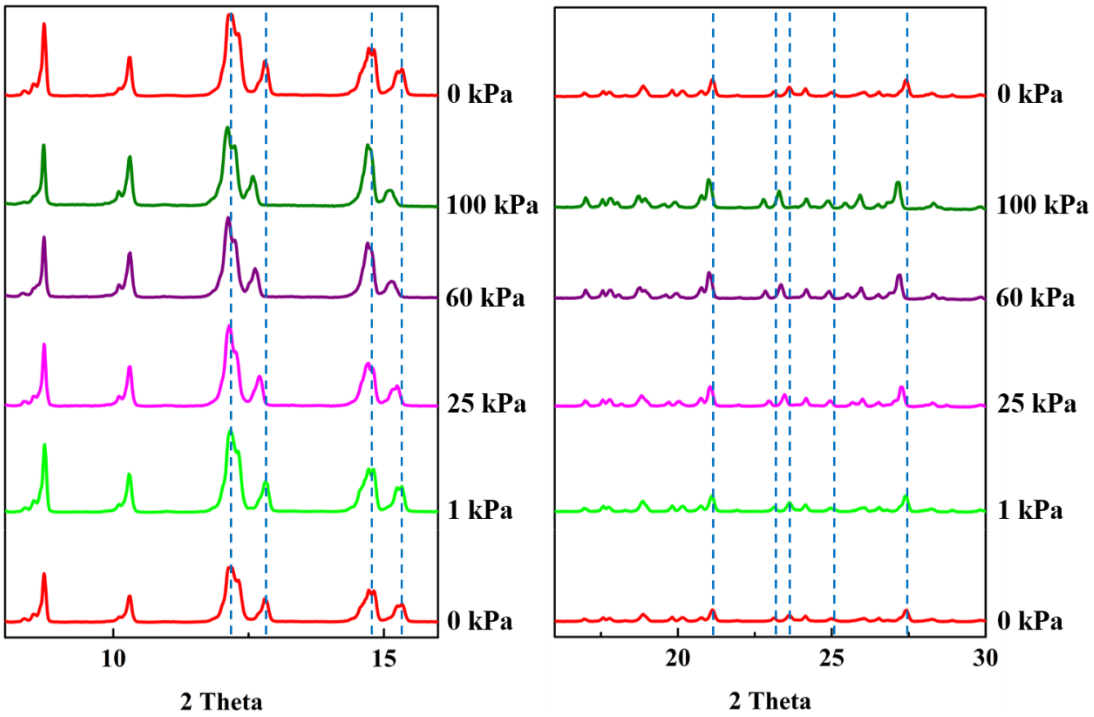

Figure S38. *In situ* powder X-ray diffraction patterns are shown for **NKU-FlexMOF-1a** at room temperature and variable C_2H_6 pressures.

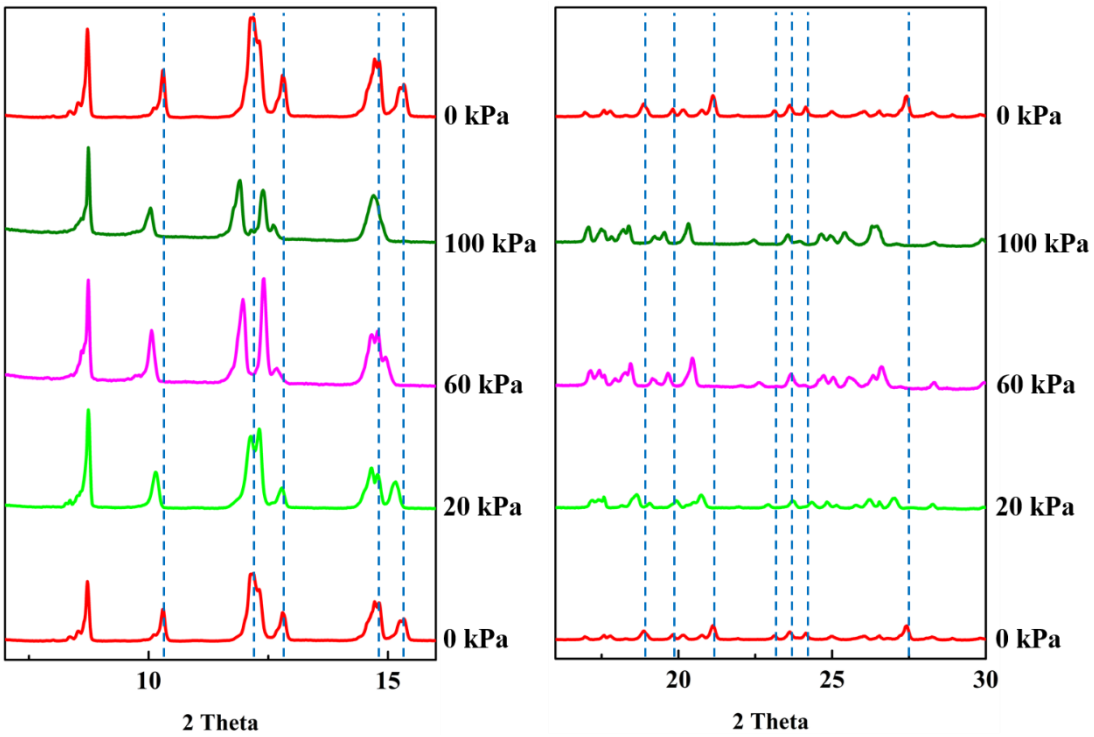

Figure S39. *In situ* powder X-ray diffraction patterns are shown for **NKU-FlexMOF-1a** at room temperature and variable C_4H_{10} pressures.

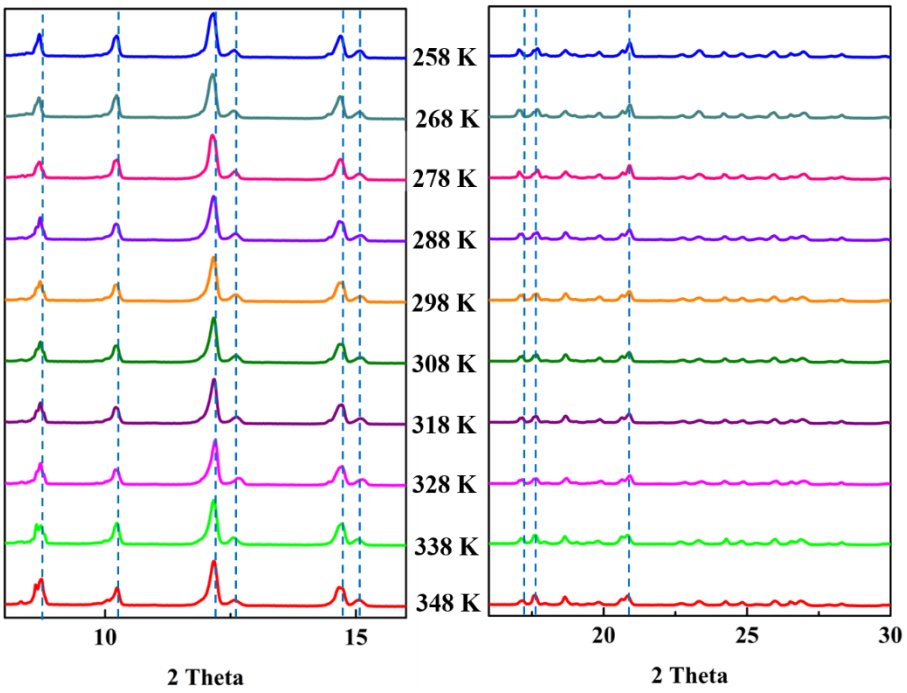

Figure S40. *In situ* powder X-ray diffraction patterns are shown for **NKU-FlexMOF-1a** loaded with propane at different temperature.

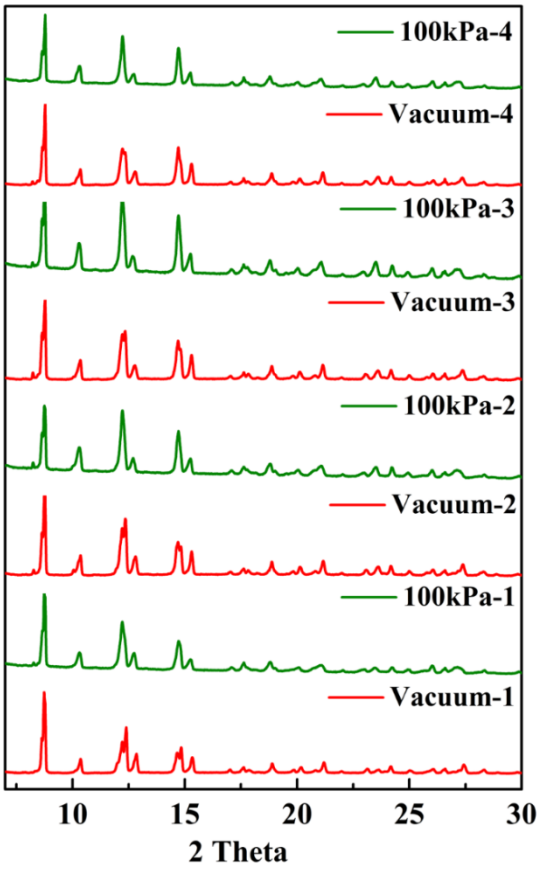

Figure S41. *In situ* powder X-ray diffraction patterns for the cyclic adsorption of C_3H_8.

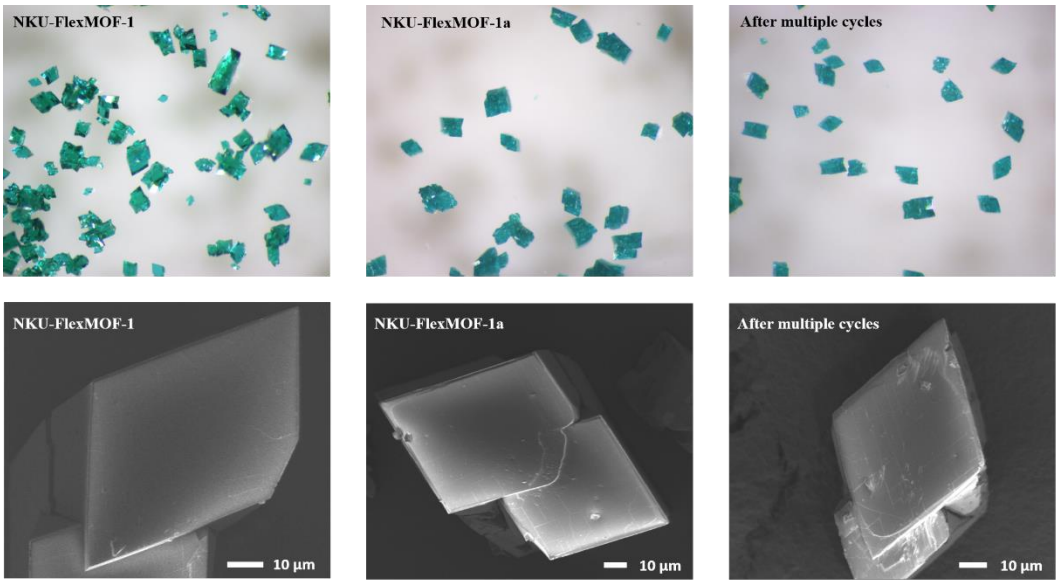

Figure S42. The morphology of the **NKU-FlexMOF-1**, **NKU-FlexMOF-1a** and the crystals after multiple cycles by optical microscopy and scanning electron microscopy (SEM).

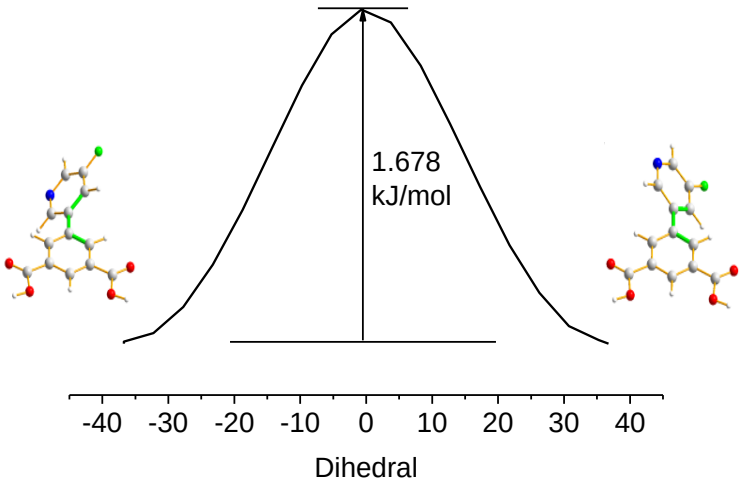

Figure S43. The torsional landscape of ligand H_2FPBDC showing the energy barrier.

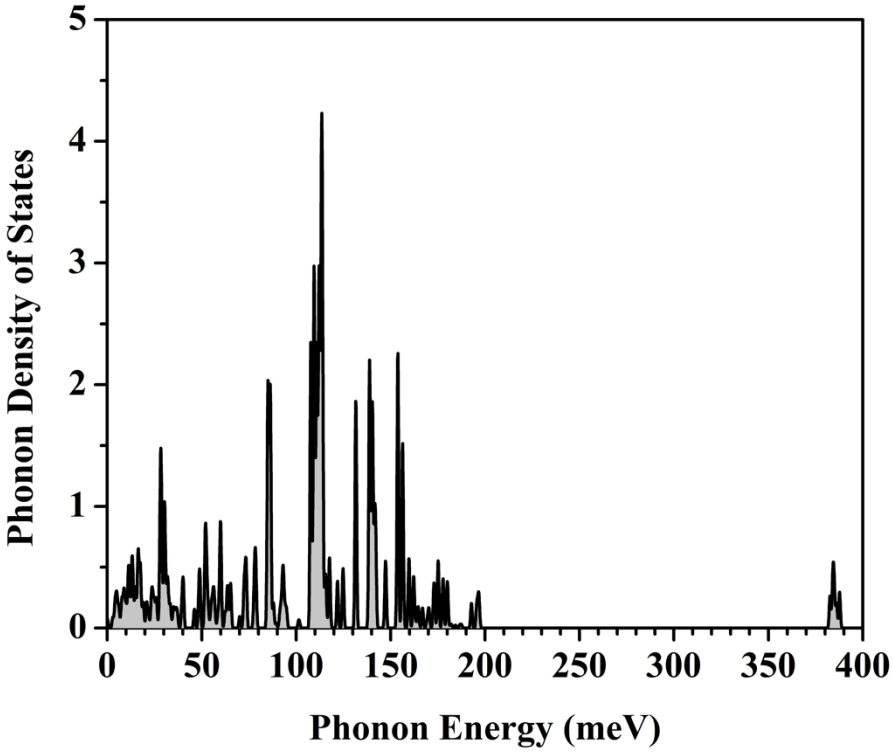

Figure S44. DFT-D calculated phonon density of states. Note that there are a number of "soft" phonon modes in the low energy region, resulted from the flexible coordination bonds. An animation of a collective coordinate with a 32 cm^{-1} frequency, involved in the relaxation, is also included in the supplementary data.

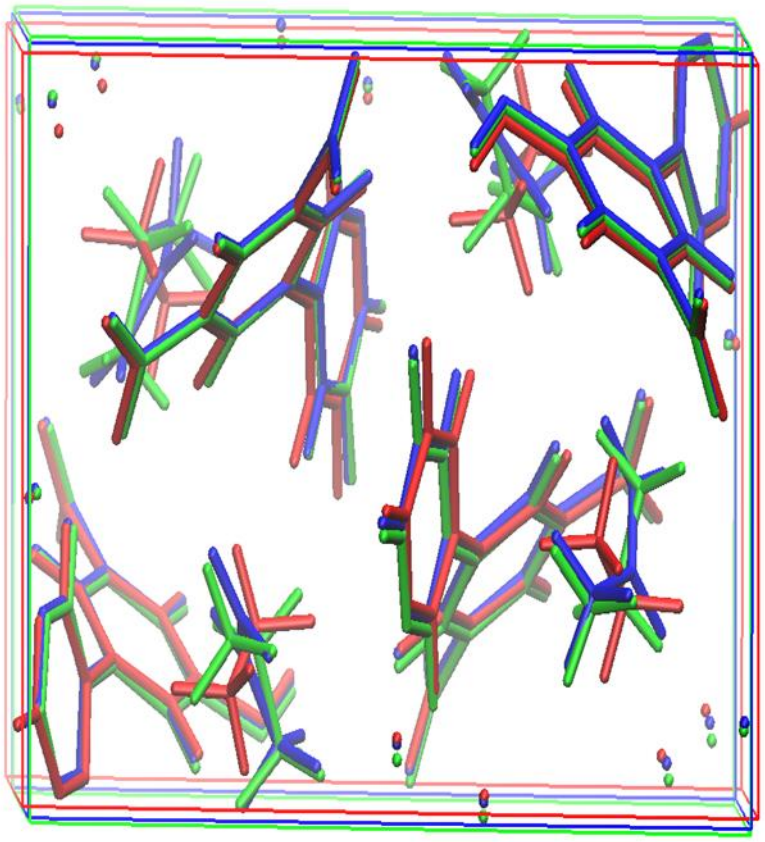

Figure S45. An overlay of the periodic DFT optimized saturated **NKU-FlexMOF-1a** systems (1x1x1 cell) with C_2H_6 (red), C_3H_8 (green), and C_3H_6 (blue), and a orthographic view down the *a* axis. The optimized unit cell box is also shown. The loaded structures are quite similar and have chemically reminiscent electrostatic environments. The structure coordinates are available upon request and are generated as described in the manuscript.

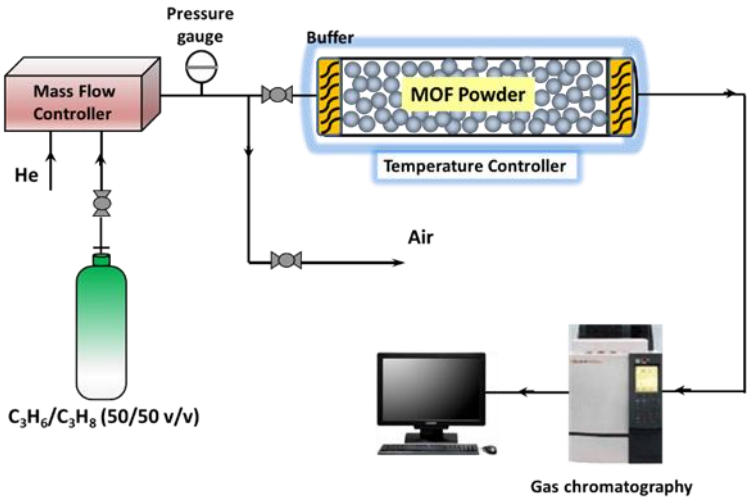

Figure S46. Schematic diagram of device of breakthrough experiments.

References

1. Giannozzi, P. et al. Quantum ESPRESSO: A modular and open-source software project for quantum simulations of materials. *J. Phys.: Condens. Matter.* **2009**, *21*, 395502.
2. Barone, V.; Casarin, M.; Forrer, D.; Pavone, M.; Sambi, M.; Vittadini, A. Role and effective treatment of dispersive forces in materials: Polyethylene and graphite crystals as test cases. *Comput. Chem.* **2009**, *30*, 934-939.
3. Kresse, G.; Furthmuller, J.; Hafner, J. Ab initio force constant approach to phonon dispersion relations of diamond and graphite. *Europhys. Lett.* **1995**, *32*, 729-734.
4. Hutter, J.; Iannuzzi, M.; Schiffmann, F.; VandeVondele, J.. CP2K: atomistic simulations of condensed mat-ter systems. *WIREs Comput. Mol. Sci.* **2014**, *4*, 15-25.
5. Rappé, K. A.; Casewit, J. C.; Colwell, S. K.; Goddard, A. W.; Skiff, M.W. UFF, a full periodic table force field for molecular me-chanics and molecular dynamics simulations. *J. Am. Chem. Soc.* **1992**, *114*, 10024-10035.
6. Krishna, R. The maxwell-stefan description of mixture diffusion in nanoporous crystalline materials. *Microporous Mesoporous Mater.* **2014**, *185*, 30-50.
7. Krishna, R. Methodologies for evaluation of metal-organic frameworks in separation applications. *RSC Adv.* **2015**, *5*, 52269-52295.
8. Krishna, R. Screening Metal-organic frameworks for mixture separations in fixed-bed adsorbers using a combined selectivity/capacity metric. *RSC Adv.* **2017**, *7*, 35724-35737.
9. Krishna, R. Methodologies for screening and selection of crystalline microporous materials in mixture separations. *Sep. Purif. Technol.* **2018**, *194*, 281-300.